Age–metallicity dependent stellar kinematics of the Milky Way disc from LAMOST and *Gaia*

Yaqian Wu [1,2]★ Maosheng Xiang,[3,1]★ Yuqin Chen,[1,4]★ Gang Zhao,[1,4] Shaolan Bi,[2] Chengdong Li,[5] Yaguang Li [6,7] and Yang Huang[8,9]

[1] *CAS Key Laboratory of Optical Astronomy, National Astronomical Observatories, Chinese Academy of Sciences, Beijing 100101, China*
[2] *Department of Astronomy, Beijing Normal University, Beijing, 100875, China*
[3] *Max-Planck Institute for Astronomy, Königstuhl 17, D-69117 Heidelberg, Germany*
[4] *School of Astronomy and Space Science, University of Chinese Academy of Sciences Beijing, 101408, China*
[5] *Rudolf Peierls Centre for Theoretical Physics, Clarendon Laboratory, Parks Road, Oxford, OX1 3PU, UK*
[6] *Sydney Institute for Astronomy (SIfA), School of Physics, University of Sydney, NSW 2006, Australia*
[7] *Stellar Astrophysics Centre, Department of Physics and Astronomy, Aarhus University, Ny Munkegade 120, DK-8000 Aarhus C, Denmark*
[8] *South West Institute For Astronomy Research, Yunnan University Kunming 650500, China*
[9] *Department of Astronomy, Peking University, Beijing, 100871, China*

ABSTRACT

We investigate the stellar kinematics of the Galactic disc in $7 < R < 13$ kpc using a sample of 118 945 red giant branch (RGB) stars from the Large Sky Area Multi-Object Fiber Spectroscopic Telescope (LAMOST) and *Gaia*. We characterize the median, dispersion and skewness of the distributions of the three-dimensional stellar velocities, actions and orbital parameters across the age–metallicity and the disc R–Z plane. Our results reveal abundant but clear stellar kinematic patterns and structures in the age–metallicity and the disc R–Z plane. The most prominent features are the strong variations of the velocity, action and orbital parameter distributions from the young, metal-rich thin disc to the old, metal-poor thick disc; a number of smaller-scale structures (such as velocity streams, north–south asymmetries, and kinematic features of spiral arms) are clearly revealed. Particularly, the skewness of V_ϕ and J_ϕ reveals a new substructure at $R \simeq 12$ kpc and $Z \simeq 0$ kpc, possibly related to dynamical effects of spiral arms in the outer disc. We further study the stellar migration by analysing the stellar orbital parameters and stellar birth radii. The results suggest that the thick disc stars near the solar radii and beyond are mostly migrated from the inner disc of $R \sim 4-6$ kpc as a result of their highly eccentrical orbits. Stellar migration resulting from dynamical processes with angular momentum transfer (churning) is prominent for both the old, metal-rich stars (outward migrators) and the young metal-poor stars (inward migrators). The spatial distribution in the R–Z plane for the inward migrators born at a Galactocentric radius of >12 kpc shows clear age stratifications, possibly evidence that these inward migrators are consequences of splashes triggered by merger events of satellite galaxies that have lasted the past few Gyr.

Key words: catalogues – disc – galaxy: fundamental parameters – galaxy: kinematics and dynamics.

1 INTRODUCTION

An interesting issue of contemporary astrophysics is our understanding of the formation and evolution of the Galactic disc. Modern large-scale sky surveys, such as the *Gaia* astrometry survey (e.g. Gaia Collaboration et al. 2016b, a, 2018; Lindegren et al. 2018), and a number of Galactic spectrocopic surveys, such as the RAdial Velocity Experiment (RAVE; Steinmetz et al. 2006), the Sloan Digital Sky Survey (SDSS; Yanny et al. 2009), the Large Sky Area Multi-Object Fiber Spectroscopic Telescope (LAMOST; Zhao et al. 2006, 2012), the Galactic Archaeology with HERMES (GALAH) survey (De Silva et al. 2015) and the Apache Point Observatory Galactic Evolution Experiment (APOGEE; Majewski et al. 2017),

have revealed unprecedented details and phenomena of our Milky Way disc through the study of the stellar distributions,[1] chemistry[2] and kinematics[3] of millions of stars. These studies have provided great insights into the structure, formation and chemo-dynamical evolution of the Galactic disc(s) (e.g. Minchev et al. 2015; Aumer &

---

[1] See, for example, Bovy et al. (2012a), Widrow et al. (2012), Mackereth et al. (2017), Xiang et al. (2018), Wang et al. (2018b) and Dobbie & Warren (2020).
[2] See, for example, Cheng et al. (2012), Hayden et al. (2014), Xiang et al. (2015a), Kawata et al. (2017), Frankel et al. (2018), Ness et al. (2018, 2019), Feuillet et al. (2019), Wang et al. (2019a) and Lian et al. (2020).
[3] See, for example, Lee et al. (2011), Bovy et al. (2012b), Carlin et al. (2013), Sun et al. (2015), Aumer, Binney & Schönrich (2017), Antoja et al. (2018), Katz et al. (2018), Kawata et al. (2018), Tian et al. (2018), Wang et al. (2018a), Bland-Hawthorn et al. (2019), Katz et al. (2019), Wang et al. (2019b), Yan et al. (2019), Coronado et al. (2020) and Li & Shen (2020).

★ E-mail: wuyaqian@mail.bnu.edu.cn (YW); mxiang@mpia-hd.mpg.de (MX); cyq@nao.cas.cn (YC)

Binney [2017](#); Ting & Rix [2019](#); Spitoni et al. [2019](#); Zhao & Chen [2020](#)).

It has been suggested that the Milky Way has two major components – the thin and the thick disc – that differ in various ways, such as spatial distribution, age, metallicity and kinematics (e.g. Gilmore & Reid [1983](#); Bensby, Feltzing & Lundström [2003](#); Spagna et al. [2010](#); Lee et al. [2011](#); Haywood et al. [2013](#); Hayden et al. [2014](#); Xiang et al. [2015a](#), [2017a](#)). Regarding kinematics, the thin disc contains stars that show larger rotation velocities and smaller velocity dispersion than the thick disc (e.g. Chiba & Beers [2000](#)). Stars in the thick disc at the solar neighbourhood are found to exhibit a positive relation between rotation velocity and metallicity, while a negative relation is found in thin disc stars (Spagna et al. [2010](#); Lee et al. [2011](#); Adibekyan et al. [2013](#); Recio-Blanco et al. [2014](#); Grieves et al. [2018](#); Peng et al. [2018](#); Wojno et al. [2018](#)). Using these differences in stellar kinematics, a star could be categorized into the thin or thick disc population (e.g. Bensby et al. [2003](#); Li & Zhao [2017](#)).

Stellar velocities are found to exhibit significant variations in both the radial and vertical directions of the Galactic disc. In the radial direction, Siebert et al. ([2011](#)) detected a radial velocity gradient in the local disc with the RAVE survey data. Sun et al. ([2015](#)) revealed a complex radial velocity pattern with significant radial variations in $8 < R < 12$ kpc with the LAMOST spectroscopic survey of the Galactic anti-centre (LSS-GAC; Liu et al. [2014](#); Yuan et al. [2015](#)). Utilizing the LAMOST data, Tian et al. ([2017](#)) also revealed the radial velocity variations in the outer disc clearly. With the *Gaia* Data Release 2 (DR2), Katz et al. ([2018](#)) revealed the complexity of the velocity field of the Galactic disc. They also observed streaming motions in V_R, V_ϕ and V_Z. With APOGEE red giant stars, Eilers et al. ([2020](#)) found clear radial velocity patterns across the whole disc of $0 < R < 20$ kpc. It has been suggested that these radial patterns are related to the perturbation induced by both the rotating bar and the spiral arms.

In the vertical direction, the velocities of stars in the outer disc show strong north–south asymmetry (e.g. Carlin et al. [2013](#); Sun et al. [2015](#)). Williams et al. ([2013](#)) and Sun et al. ([2015](#)) investigated the stellar bulk motions of the nearby disc in detail, and revealed interesting patterns such as bending, breathing and ripples. With LAMOST red clump stars, Wang et al. ([2018a](#)) suggested that the outer disc exhibits complex kinematic structures. For example, there is a high radial velocity peak at $Z \approx 0.5$ kpc, $R \approx 10$–11 kpc. The complex structures are likely to be associated with over-density in the stellar number density (e.g. Xu et al. [2015](#)) and stellar mass distribution (e.g. Xiang et al. [2018](#)). The outermost disc shows a strong warp structure (e.g. Chen et al. [2019a](#); Skowron et al. [2019](#)), which exhibits significant features in stellar velocities (Huang et al. [2018](#); Poggio et al. [2018](#); Romero-Gómez et al. [2019](#); Wang et al. [2020](#)).

Radial migration is expected to significantly alter the position of stars in the Galactic disc (Sellwood & Binney [2002](#); Roškar et al. [2008](#); Loebman et al. [2011](#); Minchev, Chiappini & Martig [2013](#); Grand & Kawata [2016](#); Anders et al. [2018](#)). Generally, it is widely suggested that there are two processes responsible for the radial migration: one is so-called blurring, which changes the stellar radial position due to epicycle motion without changing the angular momentum; the other is so-called churning, which alters the Galactocentric position of the stars due to interactions with the Galactic bar or the spiral arms without significantly changing their orbital eccentricities (e.g. Schönrich & Binney [2009](#)). Thick disc stars may have more blurring than thin disc stars because of their highly eccentrical motions. Thin disc stars, however, may suffer a strong churning effect. At the solar neighborhood, previous works

have revealed the existence of super metal-rich stars, which have metallicities exceeding the present-day interstellar medium (ISM). These stars are likely to be a consequence of the radial migration resulting from the churning process (e.g. Nordström et al. [2004](#); Boeche et al. [2013](#); Kordopatis et al. [2013](#); Xiang et al. [2015b](#); Anders et al. [2017](#); Chen et al. [2019b](#); Wang et al. [2019a](#)).

In this work, we present a study of the stellar kinematics of the Galactic disc in $7 < R < 13$ kpc with a large sample of red giant branch (RGB) stars from the LAMOST Galactic surveys. We characterize the median, dispersion and skewness of the distributions of the three-dimensional (3D) stellar velocities, actions and orbital parameters across the age–metallicity and the disc R–Z planes. We further study the blurring and churning effects by analysing the stellar orbital parameters and stellar birth radii. The paper is organized as follows. Section 2 introduces the data we adopted. Section 3 presents the velocities and actions across the age–metallicity and R–Z planes. The orbital parameters and stellar migration are investigated in Section 4, followed by conclusions in Section 5.

2 DATA

We make use of the LAMOST RGB stars from Wu et al. ([2019](#)), who estimated stellar ages and masses for 640 986 RGB stars selected from the fourth data release of the LAMOST Galactic surveys (Deng et al. [2012](#); Zhao et al. [2012](#)). The RGB stars are selected with criteria of $T_{\rm eff} < 5500$ K and $\log g < 3.8$ dex, and they are further distinguished from red clump stars using the g-mode period spacing (ΔP) derived from the LAMOST spectra with a data-driven method based on kernal principal component analysis (KPCA), taking the asterosesimic measurements from *Kepler* (Vrard, Mosser & Samadi [2016](#)) as the training set. The stellar ages and masses are also estimated with the KPCA method, using a sample of 5376 RGB stars with asteroseismic ages from Wu et al. ([2018](#)) as the training set. The typical age uncertainty is 20 per cent for stars with a spectral signal-to-noise ratio (S/N) higher than 50 per pixel. Note that the stellar ages for metal-poor stars are underestimated because of bias inherited from the training set. Here, we opt to update the age estimates by utilizing the same method as Wu et al. ([2019](#)) but removing the metal-poor stars with artificially young ages from the training set. As a result, we find that, although not perfectly, this reduces the systematics of the age estimates by about 1–2 Gyr at the metal-poor end ([Fe/H]$\lesssim -0.6$ dex).

Stellar parameters of the RGB stars, including the radial velocity V_r, effective temperature $T_{\rm eff}$, surface gravity $\log g$, metallicity [Fe/H], absolute magnitudes M_V and M_{K_s}, alpha-element to iron abundance ratio [α/Fe], C and N abundances [C/H] and [N/H], as well as extinction E_{B-V} and spectroscopic distance, are estimated with the LAMOST Stellar Parameter Pipeline at Peking University (LSP3; Xiang et al. [2015b](#), [2017a](#)), publicly available as the LAMOST value-added catalogue (Xiang et al. [2017b](#)).[4] Given a spectral S/N higher than 50, the stellar parameters yielded by LSP3 have a typical uncertainty of 4 km s^{-1} in V_r, 100 K for $T_{\rm eff}$, 0.1 dex for $\log g$, 0.3 mag for M_V and M_{K_s}, 0.1 dex for [Fe/H], [C/H] and [N/H], and better than 0.05 dex for [α/Fe] (Xiang et al. [2017b](#)).

We cross-match the LAMOST RGB sample stars with *Gaia* DR2 for astrometric parameters. Furthermore, instead of using the spectroscopic distance in the LAMOST value-added catalogue, we make use of the *Gaia* distances from Bailer-Jones et al. ([2018](#), hereafter BJ18). Given *Gaia* DR2 coordinates, proper motions, the

---

[4] http://dr4.lamost.org/doc/vac
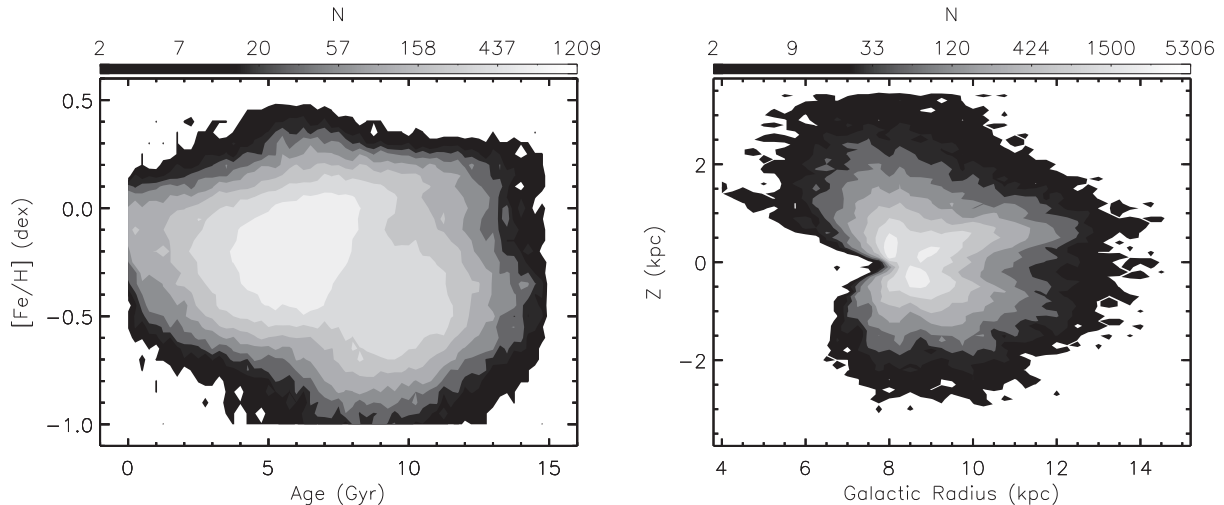
Figure 1. Colour-coded stellar number density distributions of the LAMOST RGB sample stars in the age–[Fe/H] (left) and the Galactic R–Z (right) planes. The adopted bin size is 0.25 Gyr × 0.05 dex for the age–[Fe/H] plane, and 0.1 kpc × 0.1 kpc for the R–Z plane.

BJ18 distances and the LAMOST radial velocities, we compute the Galactocentric 3D velocities (V_R, V_ϕ, V_Z) and actions (J_R, J_ϕ, J_Z), defined as the integral of the canonical momentum along the orbit

$$J_i = \frac{1}{2\pi} \oint p_i \, dx_i. \tag{1}$$

Here, p_i are the conjugate momenta: the orbital eccentricity e, epicentre R_{apo} and pericentre radii R_{peri}, minimal and maximal vertical distances from the disc, Z_{max} and Z_{min}, and guiding-centre radii R_g with GALPY (Bovy 2015), using the MWPotential2014. We adopt a right-hand Cartesian coordinate to calculate the space motions of our sample stars in cylindrical coordinates. V_R is positive for motion away from the Galactic Centre, V_ϕ is positive in the direction of Galactic rotation (note that we have changed the direction of V_ϕ, so that in this reference frame a retrograde rotation is indicated by $V_\phi < 0$ km s^{-1}) and V_Z is positive towards the North Galactic Pole. The Sun is assumed to be located at $(X, Y, Z) = (-8, 0, 0)$ kpc, and the solar motion with respect to the local standard of rest is $(U_\odot, V_\odot, W_\odot) = (7.01, 10.13, 4.95)$ km s^{-1} (Huang et al. 2015). As a result, we obtained 568 590 LAMOST–*Gaia* RGB stars with X, Y, Z, V_R, V_ϕ, V_Z, J_R, J_ϕ, J_Z, e, Z_{max}, Z_{min}, R_{apo}, R_{peri} and R_g.

To obtain a clean sample of disc stars with high quality of age estimates, we further make a few quality cuts. First of all, to ensure good age estimates, we discard stars with low spectral quality, for those of spectral S/N < 50 or stars with d_g <0.8, where d_g is an indicator of the similarity between the training and the target spectra defined in Wu et al. (2019). This cut removes 65 per cent stars in our sample. Further, we discard stars with log g < 2.0 dex, as well as stars with [Fe/H] < −1 dex, because in these parameter spaces, there is a lack of calibration stars with good seismic ages. In this work, we focus on a characterization of the observed kinematical properties of the disc stars. To minimize contamination from the halo stars, we remove stars with V_ϕ < 50 km s^{-1} from our sample. We further discard stars with parallax error larger than 20 per cent to ensure good quality of the kinematic data. Ultimately, our final sample contains 118 945 stars. Fig. 1 shows the finally adopted RGB stars in the age–[Fe/H] space and the disc R–Z plane. The left panel illustrates that the sample stars cover a wide age range, from 0 to ∼14 Gyr. For all ages, the [Fe/H] exhibits a broad distribution. For stars older than 8 Gyr, the bulk stars exhibit a negative trend between

age and [Fe/H]. The right panel illustrates that the sample covers a Galactocentric radial distance of 5–14 kpc, and a vertical distance of −3 to 3.5 kpc from the disc mid-plane. About 84 per cent of the stars are located 2 kpc from the Sun.

Fig. 2 shows the distribution of R and Z for our RGB stars in the age–[Fe/H] plane. It shows that the metal-poor young stars have a median Galactocentric radius larger than 10 kpc, while the other stars are mainly located at a Galactocentric radius not far from the solar value. In the vertical direction, as expected, the young, metal-rich thin disc stars are located close to the disc mid-plane, while the old, metal-poor thick disc stars are distributed at larger heights in general.

3 VELOCITIES AND ACTIONS

In this section, we present the distributions of velocities and actions on the age–metallicity plane in Section 3.1 and on the R–Z plane in Section 3.2.

3.1 Velocities and actions across the age–metallicity plane

We investigate the distributions of V_R, J_R, V_ϕ, J_ϕ, V_Z and J_Z for mono-age and mono-metallicity stars. In the steady state, the actions are invariant quantities describing the orbit of the star, while the velocities change along the orbit. Therefore, a comparison of the distribution patterns between velocities and actions for mono-age and mono-metallicity stars tells us information about the impact of stellar motion on the morphology of stellar distribution in the age–metallicity plane. A comparison of the two also reflects the impact of dynamical evolution due to angular momentum transfer, as the resultant alteration may differ between the velocity distribution and action distribution. For example, the 'churning' process may significantly increase the angular momentum, but may not significantly alter the rotation difference caused by orbital motion.

We divide the age–[Fe/H] plane into individual bins, and we characterize the distribution of the velocities and actions in each individual bin using three parameters: the median, the dispersion and the skewness. Here, the dispersion is defined as the standard deviation, and the skewness is defined as

$$\alpha_i = \frac{Ei^3 - 3\mu\sigma^2 - \mu^3}{\sigma^3}, \tag{2}$$
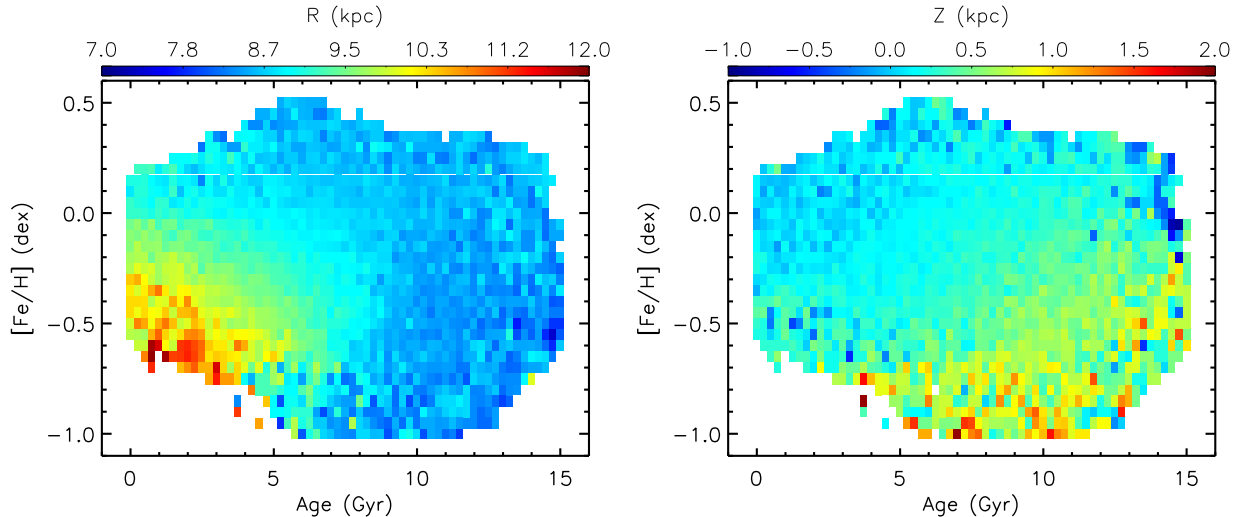
Figure 2. [Fe/H] versus age diagram for the LAMOST–*Gaia* RGB stars, colour-coded by median values of R and Z for stars in each 0.25 Gyr × 0.05 dex bin.

where μ represents the median and σ represents the standard deviation. To calculate the median, dispersion and skewness of the distribution, we adopt a bin size of 1 Gyr × 0.1 dex. We require the minimum number of stars in each bin to be at least 100. Bins with fewer stars are neglected.

3.1.1 Radial kinematics

Fig. 3 plots the results for V_R and J_R. It shows that the median values of V_R in individual bins are small ($-10 \lesssim V_R \lesssim 10\,\mathrm{km\,s^{-1}}$) across the whole age–[Fe/H] plane. There are no strong variations across the plane except for the young, metal-poor stars, which exhibit larger mean radial motion than the other stars. These young, metal-poor stars are found to be thin disc stars in the outer disc, and they also exhibit strong stream motions in the disc R–Z plane (Fig. 4). The mean J_R shows a clear separation in the age–[Fe/H] plane: the younger, more metal-rich stars exhibit small J_R, while the older, metal-poor stars exhibit large J_R. This suggests that the younger, more metal-rich stars indeed have small radial motion, whereas the old, metal-poor stars have strong radial motion, and their small mean V_R value is simply due to an average effect. Although the young, metal-poor stars have relatively large mean V_R, they have small J_R, which may be evidence that these stars have experienced perturbations. The sharp border is a good distinction between the thin and thick disc populations: the more metal-poor, older stars with larger J_R are dominated by thick disc stars, which have larger orbit eccentricities than the more metal-rich younger thin disc stars that are dominated by circular orbits, and thus small J_R (e.g. Jing et al. 2016; Mackereth et al. 2017; Feuillet et al. 2019; Yan et al. 2019). This can also be seen in Fig. 4, in which the stars with large J_R are distributed at large heights above the disc plane. For convenience, hereafter, we use the terms 'thin disc' and 'thick disc' to qualitatively represent the younger, more metal-rich stars and the older, more metal-poor stars, respectively, as separated by the border. Note that the old ($\gtrsim 10$ Gyr), metal-rich ([Fe/H] $\gtrsim 0$) stars also exhibit small V_R and J_R values, implying that these thin disc stars are co-formed with the metal-poor thick disc stars as they have comparably old ages. Finally, we note that the stellar age for thick disc stars at the metal-poor end might have been underestimated because of a lack of seismic calibration stars. However, this does not affect the main conclusions in the current

paper as the differences in the kinematics between the thin and thick disc stars are obvious.

The dispersions of both V_R and J_R exhibit a clear increasing trend from the young metal-rich stars to the old, metal-poor stars. For populations with $\tau \lesssim 8$ Gyr and [Fe/H] > 0 dex, which are mostly composed of thin disc stars, the dispersion is mainly a function of stellar age, while the trend with [Fe/H] is not obvious. Because there are strong radial metallicity gradients for these relatively young stellar populations (e.g. Xiang et al. 2015a; Anders et al. 2017), a lack of trend with [Fe/H] implies that the dispersion for mono-age and mono-metallicity stellar populations does not change significantly with Galactocentric radius. This conclusion can also be reached by combining Fig. 3 with Fig. 2, which shows that the stars with age < 5 Gyr and [Fe/H] < -0.2 dex have a mean Galactocentric radius beyond 10 kpc, while the stars with solar metallicity at the same age mainly locate at $\sim$8 kpc. Such a lack of radial variations in V_R and J_R is probably related to the bifurcation structure in the V_R distribution of the stars in the outer disc (Liu et al. 2012; Sun et al. 2015), as these bifurcation structures will increase the measured dispersions at the outer disc and thus the metal-poor bins of a given age.

The skewness of V_R is $\sim$0 and it uniformly distributes across the age–[Fe/H] plane, indicating that, for all mono-age and mono-abundance bins, V_R follows nearly Gaussian distributions (see Fig. A1 in the Appendix). However, the skewness in J_R shows strong patterns, as the young, metal-rich stars show much larger positive skewness than the old, metal-poor stars. Note that, given the definition of J_R, the skewness is always positive (Fig. A1). Interestingly, Fig. 3 shows that the skewness of the old, metal-rich stars is different from that of the young metal-rich stars but similar to the old, metal-poor stars, in contrast to the case of mean J_R. We find that the J_R distribution for the old, metal-rich stars is more dispersed than the young, metal-rich stars. This makes the skewness of the old, metal-rich stars lower than that of the young metal-rich stars.

3.1.2 Azimuthal kinematics

Fig. 5 plots the results of V_ϕ and J_ϕ. It shows that the median V_ϕ and J_ϕ are clearly different between the younger, more metal-rich thin disc stars and the older, more metal-poor thick disc stars, because the latter have lower rotation velocities and angular momentum. The sharp border between the two overall populations (i.e. the thin
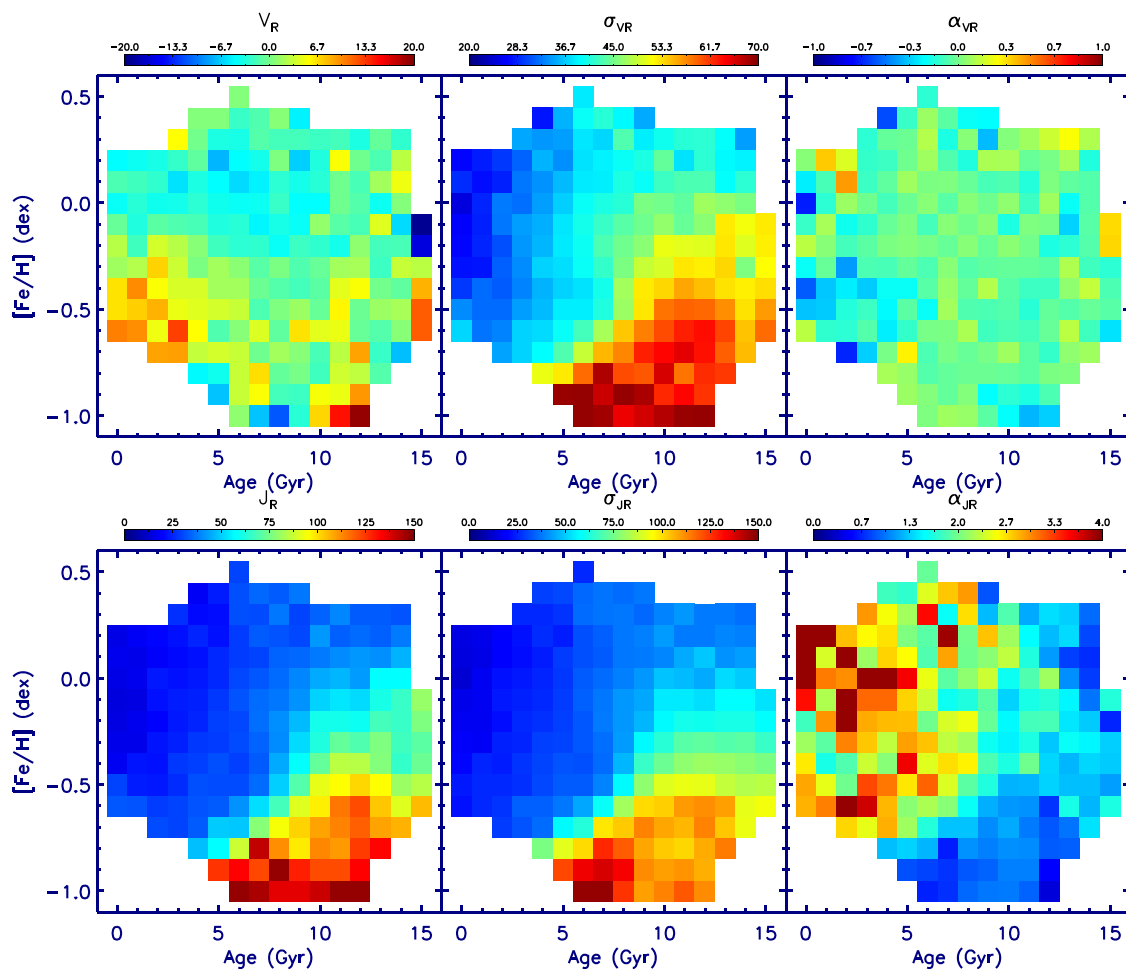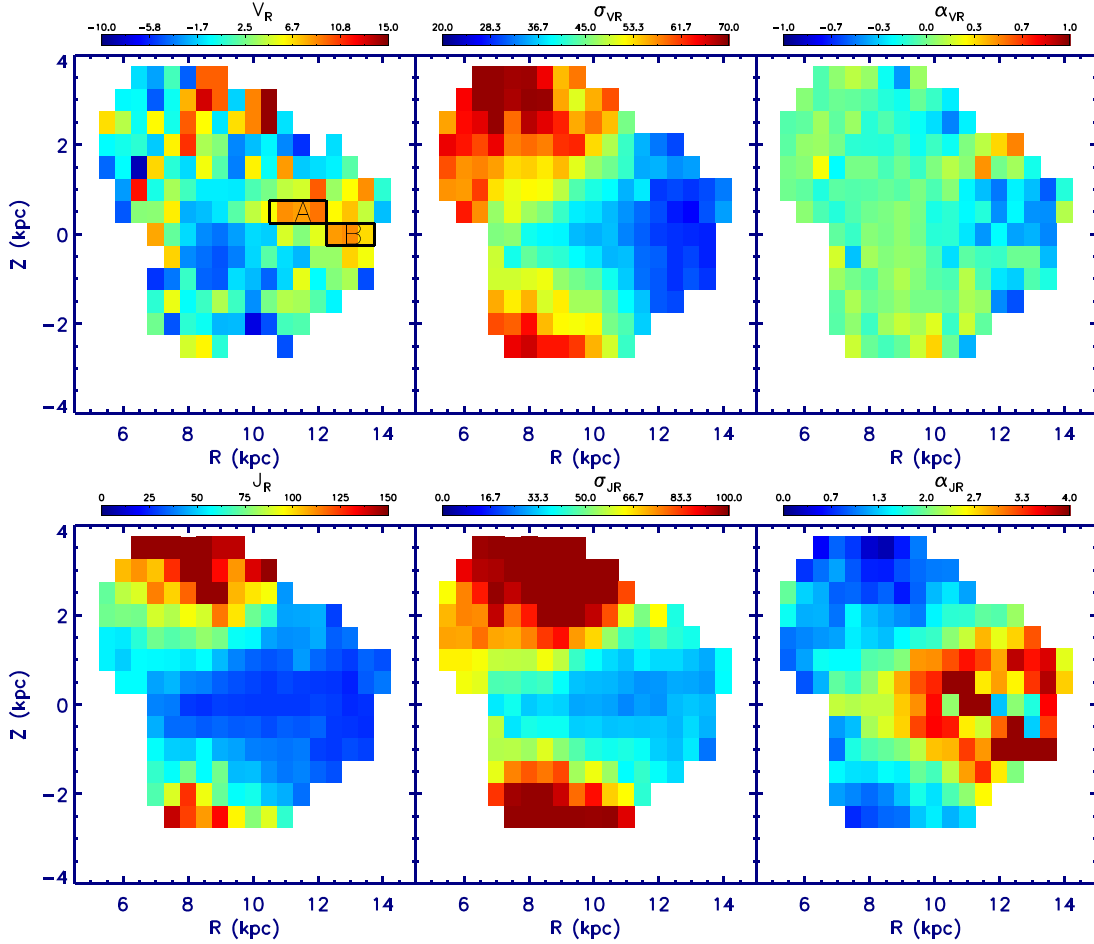
Figure 3. Distributions of the LAMOST–*Gaia* RGB stars in the age–[Fe/H] plane, colour-coded by the values of median (left-hand panels), dispersion (middle panels) and skewness (right-hand panels) of the distribution functions of the radial velocity (V_R) and action (J_R) for stars in each 1.0 Gyr × 0.1 dex age–[Fe/H] bin.

disc and the thick disc) is consistent with Fig. 3. For the thin disc stars, the values of V_ϕ and J_ϕ increase with decreasing [Fe/H]. In contrast, the values for V_ϕ and J_ϕ of thick disc stars exhibit a positive trend with [Fe/H]. This is consistent with previous results (Spagna et al. 2010; Lee et al. 2011; Adibekyan et al. 2013; Recio-Blanco et al. 2014; Allende Prieto, Kawata & Cropper 2016; Peng et al. 2018; Yan et al. 2019). The figure shows this negative trend for thin disc stars of all mono-age stellar populations of $\tau \lesssim 7$ Gyr. The reason for such a negative trend between V_ϕ and [Fe/H] is likely a combined consequence of the stellar migration due to epicycle motion and the negative radial metallicity gradients of the Galactic disc. That is to say, the outer, metal-poor stars are mainly inward migrators, at the pericentre phase of their orbits (see Section 4) and with large V_ϕ, while the inner/solar neighbourhood, metal-rich stars are mainly outward migrators, at the apocentre phase of their orbits and with small V_ϕ (see Loebman et al. 2011; Curir et al. 2012; Minchev et al. 2015; Kawata et al. 2018). For the thick disc stars, the positive trend between V_ϕ and [Fe/H] is likely a consequence of a negative vertical metallicity gradient (e.g. Curir et al. 2012; Xiang et al. 2015a; Anders et al. 2017; Kawata et al. 2018) and the stellar migration. The more metal-poor thick disc stars are generally at larger heights and have smaller V_ϕ, either because they were born hotter so that they have larger eccentricity and/or because the thick disc was born with a positive radial metallicity gradient (e.g. Curir,

Mazzei & Murante 2004). For a given [Fe/H], younger stars have generally larger V_ϕ or J_ϕ, which is consistent with the fact that older stars exhibit more dynamical evolution (e.g. Ting & Rix 2019). Note that at the metal-poor and $\tau < 5$ Gyr region, the data present a sharp boundary that exhibits a negative trend between [Fe/H] and age. This is likely a consequence of Galactic chemical enrichment with time (e.g. Schönrich & Binney 2009). This effect also causes a steeper V_ϕ–[Fe/H] gradient for the younger population.

The dispersions of V_ϕ and J_ϕ also exhibit a clear increasing trend from the younger, more metal-rich stars to the older, more metal-poor stars. For the thin disc population, the dispersion of V_ϕ does not change significantly with [Fe/H], indicating that the value for σ_{V_ϕ} is nearly constant along the Galactocentric radius for the mono-age stellar population. However, the value of σ_{J_ϕ} at a given age increases with decreasing [Fe/H]. This is simply a consequence of constant σ_{V_ϕ} and the fact that the more metal-poor stars are located at a larger Galactocentric radius.

The skewness of V_ϕ is mostly negative for thin disc stars and ~ 0 for thick disc stars. This means that the V_ϕ distribution for the thin disc stars has a negative tail, which is largely contributed by stars in the outer disc (i.e. with larger R). While the V_ϕ distribution for the thick disc stars is nearly Gaussian. The skewness of J_ϕ is close to zero in the majority of the age–[Fe/H] bins, even for many for which the V_ϕ skewness is negative. This is not surprising, because some

Figure 4. Distributions of the LAMOST RGB stars in the Galactic R–Z plane. Colours represent the median (left-hand panels), dispersion (middle panels) and skewness (right-hand panels) of the radial velocities and action distribution functions for stars in each $0.5 \times 0.5 \, \mathrm{kpc}^2$ bin. The substructures (A and B) with high V_R values are marked in the top-left panel (see text).

of stars in the negative tail of V_ϕ are located at larger R, so that the J_ϕ ($=V_\phi \times R$) distribution will not exhibit a similar negative tail to V_ϕ. Nonetheless, for some age–[Fe/H] bins of $\tau < 5 \, \mathrm{Gyr}$, [Fe/H] $\sim$ $-0.6 \, \mathrm{dex}$, the stars exhibit strong negative skewness in J_ϕ, possibly due to spiral arm dynamics (Wu et al., in preparation; see also Kawata et al. 2018).

3.1.3 Vertical kinematics

Fig. 6 shows that the median value of V_Z is generally small ($-5 \lesssim V_Z \lesssim 5 \, \mathrm{km \, s^{-1}}$), and largely across the whole age–[Fe/H] plane expect for the young, metal-poor stars, which exhibit systematically positive mean motion. The value of J_Z exhibits a clear increasing trend from the younger, metal-rich thin disc stars to the older, metal-poor thick disc stars, and there is a clear border between the thin and thick disc stars.

The dispersion of V_Z increases smoothly with both age and [Fe/H]. For stars with the same age, the velocity dispersion increases as [Fe/H] decreases. At a given [Fe/H], the dispersion of V_Z increases with age for thin disc stars. This relation is known as the age–velocity dispersion relation (AVR), and the results are consistent with previous works (e.g. Holmberg, Nordström & Andersen 2009; Tian et al. 2015; Hayden et al. 2017, 2020). It is suggested that the observed AVR of the thin disc stars is a consequence of gradual

heating through the scattering process, and that the stars were born with a roughly constant velocity dispersion smaller than $10 \, \mathrm{km \, s^{-1}}$ (Aumer & Binney 2009; Ting & Rix 2019). Similar to the case of mean J_Z, the dispersion of J_Z shows a sharp border between the younger, more metal-rich stars and the older, more metal-poor stars.

Similar to the case of mean V_Z, the skewness of V_Z is also ~ 0 and uniformly distributes across the age–[Fe/H] plane, indicating that for all mono-age and mono-abundance bins, V_Z follows nearly Gaussian distributions (Fig. A1). The skewness of J_Z shows strong patterns, as the young metal-rich populations show larger positive skewness than the old, metal-poor populations. Note that given the definition of J_Z, the skewness is also always positive (Fig. A1).

3.2 Kinematics across the *R*–*Z* plane

3.2.1 Radial velocity V_R and action J_R

Fig. 4 plots the results of V_R and J_R across the R–Z plane. To calculate the median, dispersion and skewness of the distribution, we adopt a bin size of $0.5 \times 0.5 \, \mathrm{kpc}^2$. We further require a minimal number of 100 in each bin, and we discard bins with fewer stars. The mean V_R shows irregular substructures. At the solar radius of $7 < R < 9 \, \mathrm{kpc}$, and $|Z| < 0.5 \, \mathrm{kpc}$, stars with $R < 8 \, \mathrm{kpc}$ move outwards (with positive velocity), while stars with $R > 8 \, \mathrm{kpc}$ move inwards (with negative velocity). This shows a negative radial velocity gradient
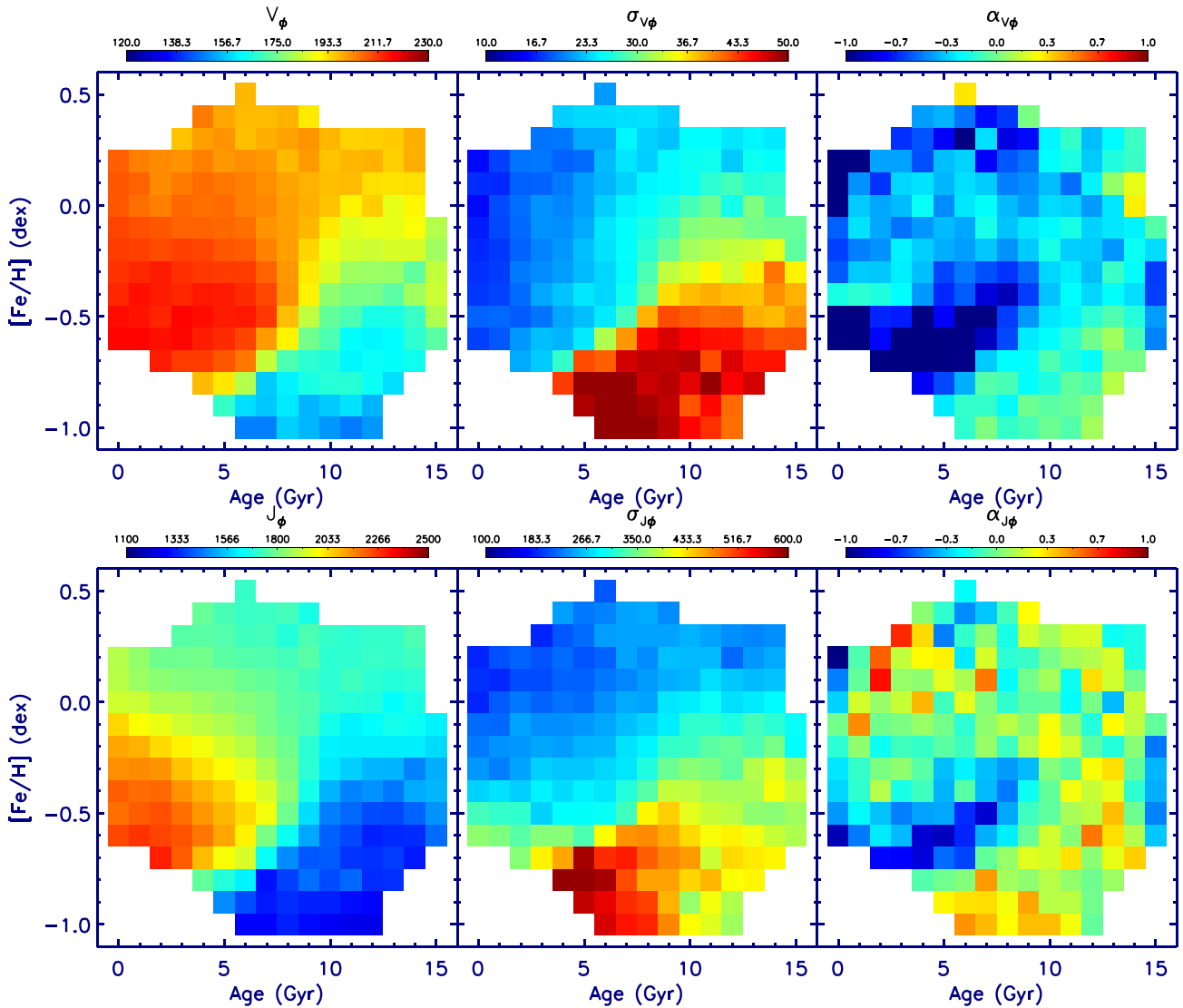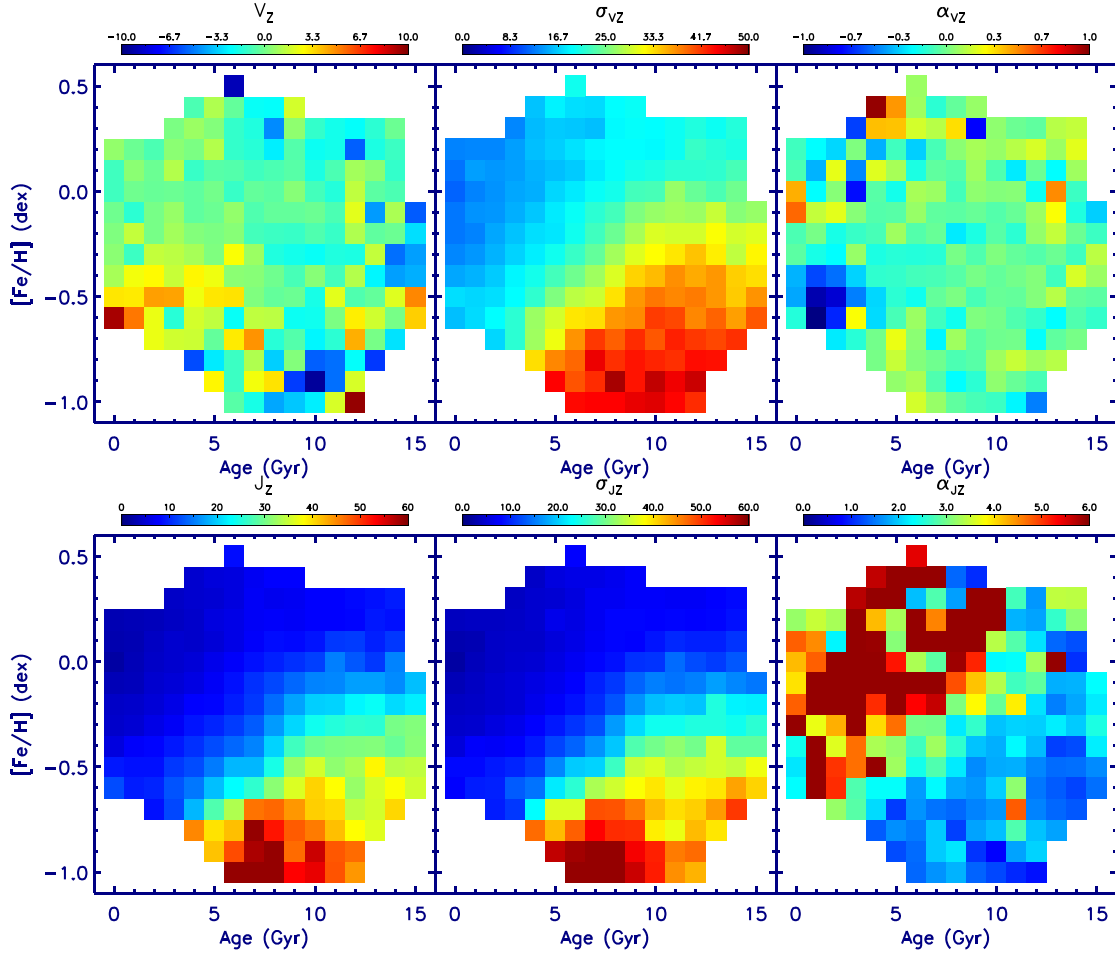
Figure 5. Same as Fig. 3, but for the azimuthal component of the stellar velocities and actions.

in the solar radius. Utilizing the RAVE data, Siebert et al. (2011) measured a negative radial velocity gradient from about 2 kpc inside the Sun to about 1 kpc outside. Williams et al. (2013) confirmed the negative radial velocity gradient using RAVE red clump stars. With LAMOST red clump stars, Tian et al. (2017) and Wang et al. (2018b) found that the radial velocity is oscillating along R, as the value is negative at $R < 9$ kpc but becomes positive beyond $R \sim 9$ kpc. These patterns were also revealed by Katz et al. (2018). In the outer disc, the most prominent features are those with positive V_R in $10 < R < 14$ kpc. There are two positive velocity peaks, one at $10 \lesssim R \lesssim 12$ kpc and $Z \sim 0.5$ kpc, the other at $R \sim 13$ kpc and $Z \sim 0$ kpc. These substructures in the outer disc correspond to those presented in Fig. 3 for young, metal-poor stars. In Fig. 7, we slice the stars into age bins to show how these V_R structures vary with age. The figure illustrates that the substructure with positive V_R at the outer disc of $Z \sim 0.5$ kpc is strong for young stellar populations, and is also present in old populations. This structure is likely related to the so-called 'north-near' overdensity/stream presented in previous works (Xu et al. 2015; Wang et al. 2018b; Xiang et al. 2018). The peaks at $R \sim 13$ kpc and $Z \sim 0$ kpc occurs in the age bin of 3–6 Gyr, but

it is hard to tell if they are also present in other age bins because of the limited spatial coverage of the data – but see Wang et al. (2019b) for velocity structure in the outermost disc of $R > 12$ kpc. The J_R distribution exhibits a flaring structure in the outer disc, and the J_R values are small near the Galactic plane across the whole radii. In contrast, the stars with $R < 10$ kpc and $|Z| \gtrsim 1$ kpc exhibit large J_R values, suggesting that stars at those high Galactic latitude, mostly thick disc stars, have strong radial motions.

The dispersion of V_R and J_R exhibits a strong flaring structure across the whole radial range from $R \sim 6$ kpc to $R \sim 13$ kpc, with larger dispersion at larger heights. At $|Z| < 1$ kpc, the dispersion of V_R decreases significantly with increasing Galactic radius, which is likely driven by the age of the stellar populations (i.e. the outer disc is dominated by younger stars).

The skewness of V_R is close to 0 across the R–Z plane, except for the outer disc region of $R \gtrsim 11$ kpc, which shows negative skewness, possibly caused by the strong substructures with positive V_R. The value of J_R for stars at low Galactic heights or in the outer disc, mostly thin disc stars, exhibits strong positive skewness because of the sharp distributions (see also Fig. 3 and the explanations in Section 3.1.1).

Figure 6. Same as Fig. 3, but for the vertical component of the stellar velocities and actions.

3.2.2 Azimuthal velocity V_ϕ and action J_ϕ

Fig. 8 plots the results of V_ϕ and J_ϕ across the *R–Z* plane. It shows a clear vertical gradient on both sides of the disc that represents the transition from the thin to the thick disc. The V_ϕ of the thin disc exhibits a flaring structure. In the outer disc of $R \geq 10$ kpc and $|Z| \geq 0.5$ kpc, stars in the south are rotating faster than those at the symmetric positions in the north, which is consistent with previous findings of Wang et al. (2018b). J_ϕ shows regularized flaring patterns across the whole disc covered by our data, a consequence of the increase of Galactocentric radius and the vertical V_ϕ gradient, as the former causes larger J_ϕ at the outer disc while the latter causes smaller J_ϕ at larger heights.

The dispersion of V_ϕ and J_ϕ also exhibits a clear increasing trend from smaller heights to larger heights. For the thin disc stars, the dispersion of V_ϕ exhibits a clear flaring structure (i.e. stars at larger $|Z|$ or smaller R have larger V_ϕ dispersion). As a consequence, the dispersion of J_ϕ is largely invariant with R. However, for the thick disc stars, the dispersion of V_ϕ is largely invariant with R. As a consequence, the dispersion of J_ϕ increases significantly with R in the thick disc.

The skewness of V_ϕ and J_ϕ is generally negative for thin disc stars and ~ 0 for thick disc stars. Interestingly, in $11 < R < 13$ kpc, $-0.25 \lesssim Z \lesssim 0.25$ kpc, the skewness of V_ϕ and J_ϕ is clearly different from the other regions nearby. We find that there are bifurcations in the J_ϕ distribution that are probably an effect of spiral arms. Detailed discussions on this structure will be presented in Wu et al. (in preparation).

3.2.3 Vertical velocity V_Z and action J_Z

Fig. 9 plots the results of V_Z and J_Z across the *R–Z* plane. It shows that stars in the north and south sides of the plane at $R \sim 8.5$ kpc exhibit net upward vertical motions. This is the bending mode (Widrow et al. 2012, 2014; Williams et al. 2013; Sun et al. 2015; Carrillo et al. 2018; Chequers, Widrow & Darling 2018), and the results are similar to the results shown by Williams et al. (2013), Carrillo et al. (2018) and Wang et al. (2019b). At the outer disc $R \sim 13$ kpc, it is revealed that the vertical velocities in southern disc stars have larger vertical velocities than the northern disc stars, due to the effect of the warp structure (Chen et al. 2019b; Skowron et al. 2019). The values for J_Z show a strong dependence on Z while they are only marginally dependent on R. This is determined by the nature of J_Z. As J_Z quantifies the vertical excursions of an orbit, and vanishes for orbits lying entirely in the Galactic plane, stars at large heights have large vertical excursions, while stars near the plane have large probabilities to be with small vertical excursions.

The dispersion of V_Z exhibits a clear flaring structure, which shows a negative radial gradient and a positive vertical gradient. The negative radial gradient of σ_{V_Z} is expected because σ_{V_Z} is associated with the surface mass density (e.g. Freeman & Bland-Hawthorn 2002; Binney & Tremaine 2008), which decreases with increasing Galactocentric radius (e.g. Xiang et al. 2018). The positive vertical gradient mainly reflects the increase of surface mass density enclosed by increasing height above the disc. The dispersion of J_Z, however,
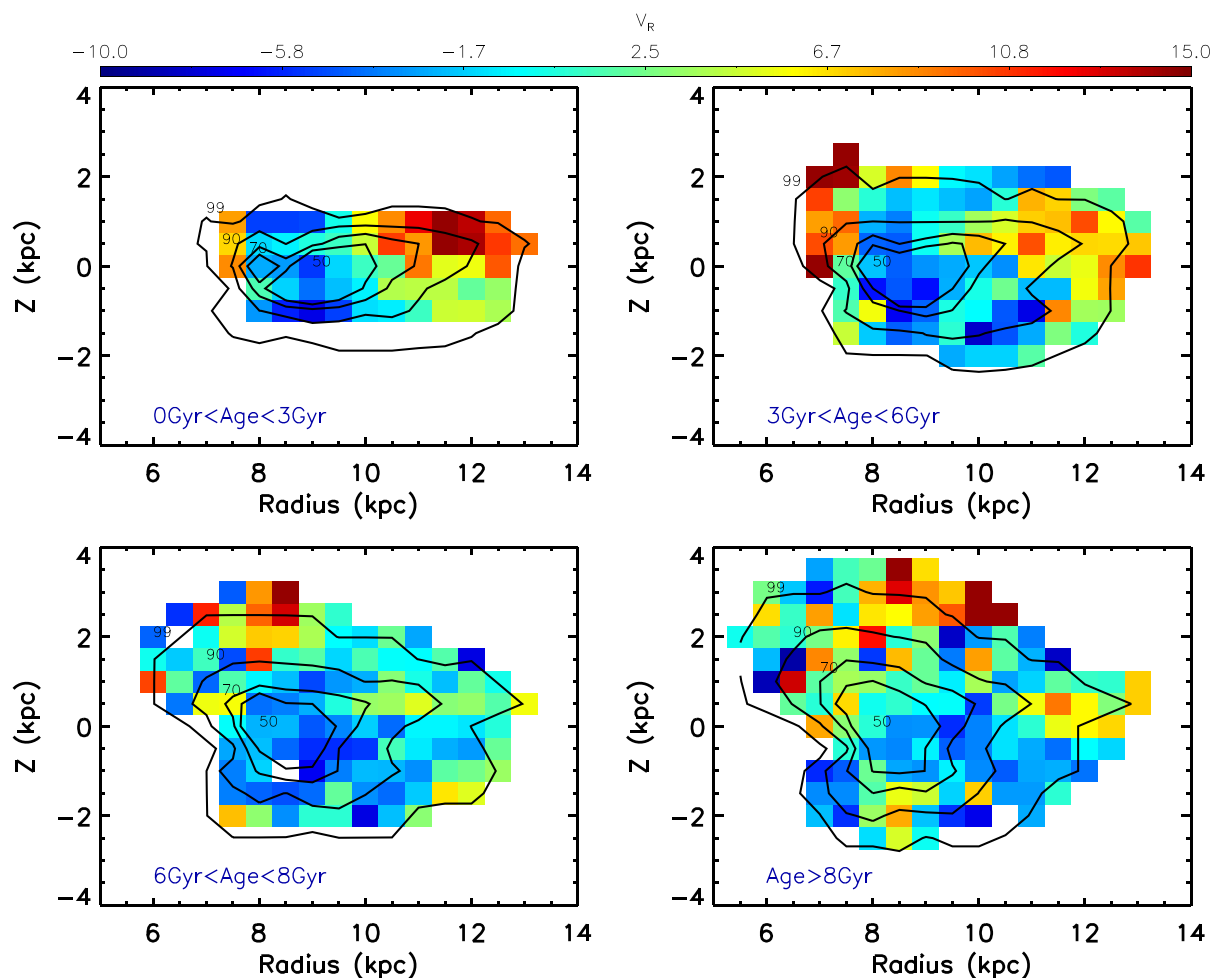
Figure 7. Colour-coded distributions of median V_R across the distance R–Z plane for stars in different age bins. Also shown are the contours indicating 50, 70, 90 and 99 per cent of the sample stars.

has less dependence with R. Again, this is likely to be because of the nature of J_Z, as discussed above.

The skewness of V_Z is close to 0 and uniformly distributes across the R–Z plane, except for the outermost region ($R > 11$ kpc), whereas the skewness in J_Z shows strong patterns. These characteristics are similar to the case of skewness for V_R and J_R, and they share similar physical reasons (see Section 3.2.1).

4 ORBITAL PARAMETERS AND STELLAR MIGRATION

In this section, we present the orbital parameters of the RGB stars across the age–metallicity plane and the disc R–Z plane. We discuss the impact of non-circular orbital motion on the stellar distribution by comparing the current position of the stars with the guiding-centre radii of their orbits. We further estimate the birth radii of the stars based on their age and metallicity in the same way as Chen et al. (2019b), initially proposed by Minchev et al. (2018), and we study the effect of stellar migration (churning). Note that here we refer to the stellar migration as the churning process, in which stars change their orbital radii through angular momentum transfer via scattering or perturbation (e.g. Sellwood & Binney 2002; Minchev et al. 2013).

4.1 Orbital parameters

As mentioned in Section 2, the orbital parameters of our sample stars are derived using positions and proper motions from *Gaia* DR2, distances from BJ18 and radial velocities from LAMOST DR4. The orbit calculation is implemented with GALPY, assuming the MWpotential2014 (Bovy 2015).

Fig. 10 plots the median, dispersion and skewness of the stellar eccentricity distributions in the age–[Fe/H] plane and the disc R–Z plane. The figure illustrates that the young or old but metal-rich thin disc stars have mean orbital eccentricities smaller than 0.2, and have small (<0.1) dispersion among stars in each mono-age and mono-[Fe/H] bin, which is consistent with previous work (e.g. Kordopatis et al. 2015). The old, metal-poor thick disc stars have larger eccentricities and broader distribution, and their mean eccentricities vary from 0.2 to larger than 0.5. For the thin disc stars, the eccentricity steadily increases with stellar age and exhibits little change with [Fe/H] at a fixed age, possibly suggesting that the steady disc heating processes have played a decisive role in determining the orbital evolution of these stars (e.g. Ting & Rix 2019). At a given age, the [Fe/H] of a star is an indicator of its Galactocentric radius because of the existence of radial [Fe/H] gradient for mono-age populations (e.g. Boeche et al. 2013; Xiang et al. 2015a, 2017a; Anders et al. 2017; Wang et al. 2019a). The lack of variations with [Fe/H] suggests that the overall eccentricity for stars with the same
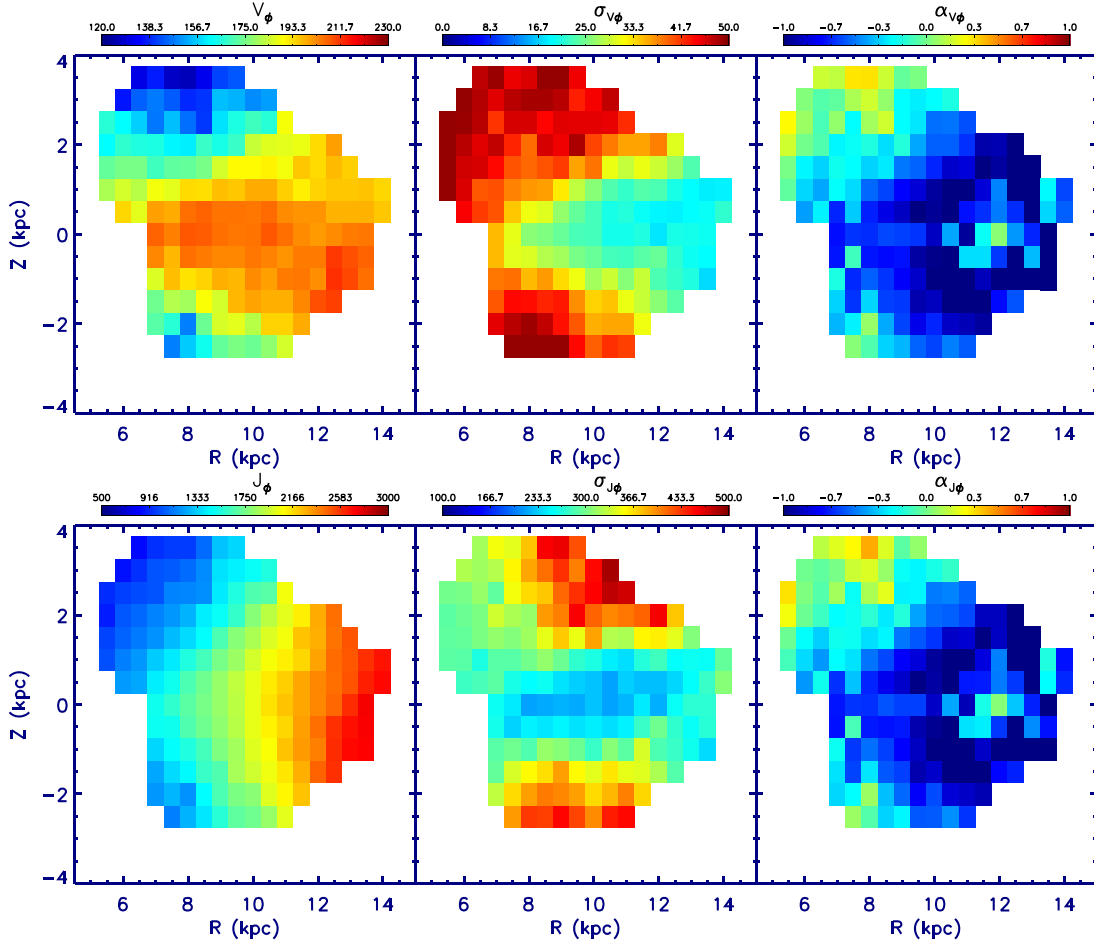
Figure 8. Same as Fig. 6, but for the azimuthal component of the stellar velocities and actions.

age has few radial variations in the range of our sample ($7 < R < 13$ kpc). The spatial patterns of eccentricity in the R–Z plane reflect mainly the superposition of stellar populations of different ages. The young, outer disc stars exhibit positive skewness. The patterns in both the age–[Fe/H] and R–Z planes are similar to the inverse cases for V_ϕ (see Figs 5 and 8). This is expected as the eccentricity is largely determined by V_ϕ. Interestingly, in $11 < R < 13$ kpc, $-0.25 \lesssim Z \lesssim 0.25$ kpc, the dispersion and skewness of eccentricity exhibit peculiar behaviours, similar to the case of V_ϕ. This is might be an effect caused by spiral arms (Wu et al., in preparation).

Fig. 11 plots the distributions of Z_{max}, R_g, R_{peri} and R_{apo}. The figure clearly shows that the younger, more metal-rich stars have maximal orbital heights smaller than 1 kpc, while the older, metal-poor stars have maximal orbital heights larger than 1 kpc, giving credence to our definition of 'thin' and 'thick' disc populations in Section 3. The thick disc stars have orbital guiding-centre radii of 4–6 kpc, pericentre radii of 3–6 kpc and apocentre radii of <10 kpc. This is consistent with the convention that thick disc stars are all formed in the inner disc (e.g. Haywood et al. 2013). It is clear that the thick disc stars exhibit smaller guiding-centre radii than the thin disc stars. The figure also illustrates that, except for the young, metal-poor ones, stars in all age and [Fe/H] bins have apocentre radii $\simeq 10$ kpc. In other words, the 'inner' ($R_{apo} < 10$ kpc) disc has complex stellar populations, which dominate most of the age–[Fe/H] space, while the 'outer' ($R_{apo} > 10$ kpc) disc has a relatively simple formation history, as the stars dominate only a small, specific part of the age–[Fe/H] space.

4.2 Non-circular motion

Because of the non-circular nature of stellar orbits, stars change their radial positions along the orbits without changing the angular momentum. Here we study the impact of non-circular effect on the stellar distribution by comparing the current radial position (R) of the star with their orbital guiding-centre radii (R_g). Fig. 12 shows the distributions of median value of $R - R_g$ for stars across the age–metallicity and R–Z planes. The figure shows a sharp border between the younger, metal-rich thin disc stars and the older, metal-poor thick disc stars: the thick disc stars show positive values of 1–4 kpc, indicating that they are currently at their apocentre side. This is a strong non-circular effect considering the fact that 4 kpc is comparable to their guiding-centre radii (Fig. 11). However, the thin disc stars exhibit only a small effect, as $R - R_g$ has a value of only -1 kpc to ~ 1 kpc, depending on the location in the age–[Fe/H] and R–Z planes. The young, metal-poor stars at the outermost disc ($R > 12$ kpc, $Z < 0$ kpc) exhibit a strongest negative $R - R_g$ of about -1 kpc. Note that these stars belong to the warp structure of the outer disc in the third quadrant. The negative $R - R_g$ values suggest that these stars are currently at the pericentre side of their orbits.

4.3 Churning

The determination of the stellar churning effect relies on knowledge about the stellar birth radii. This is a tough task, as the stellar kinematics themselves tell little about the birth position of a migrator.
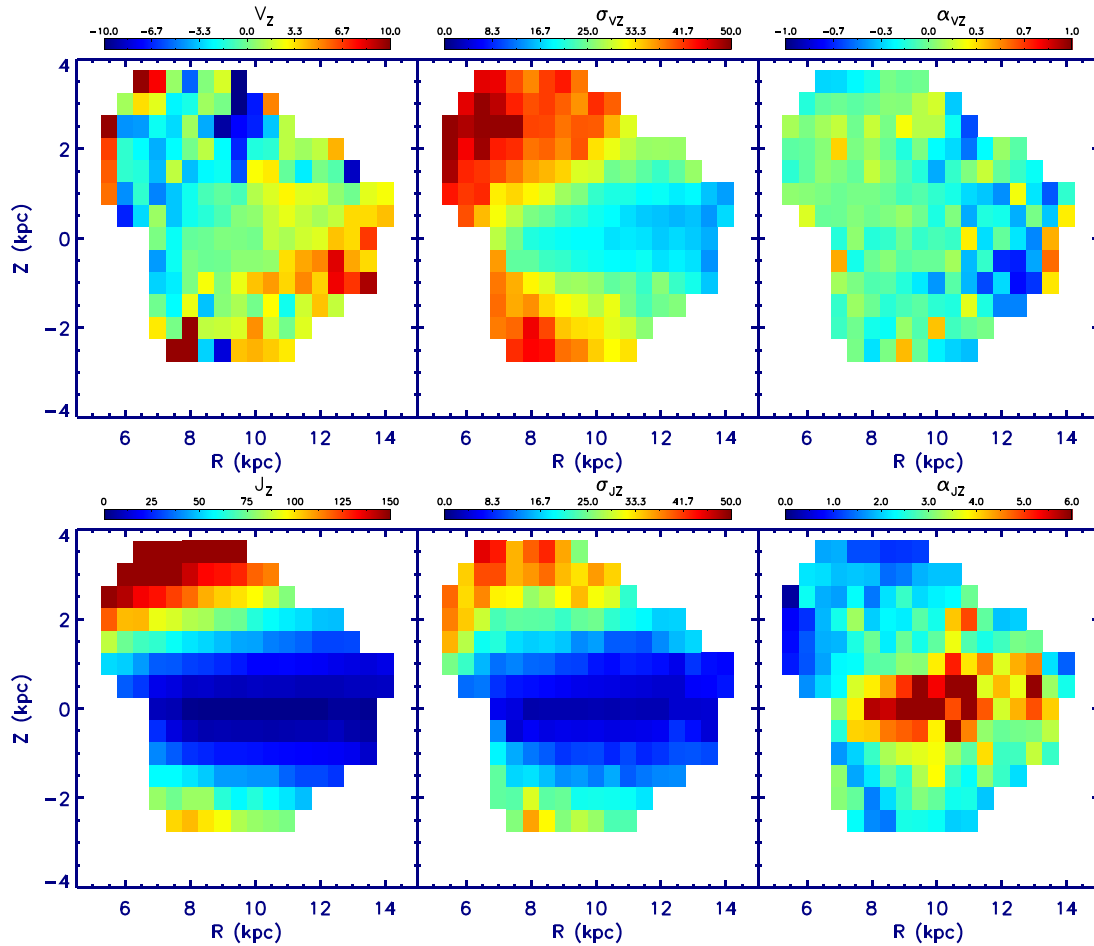
Figure 9. Same as Fig. 6, but for the vertical component of the stellar velocities and actions.

It has been suggested that, for some particular stellar populations, the stellar metallicity, as a fossil record for metallicity of the ISM from which the star was born, can be an indicator of the stellar birth place. For example, old ($\gtrsim 8$ Gyr), metal-rich ([Fe/H] > 0) stars are generally expected to be formed at the inner part of the thin disc. So, if such stars occur at the solar neighbourhood or the outer disc with near circular orbits, they are likely to have arrived at their current position via churning (e.g. Nordström et al. 2004; Schönrich & Binney 2009; Boeche et al. 2013; Kordopatis et al. 2013; Chen et al. 2019b; Wang et al. 2019a).

With the justifiable assumption that a negative radial metallicity gradient in the ISM has existed for most of the disc's lifetime, and that the dispersion of the ISM metallicity at a given age and radius is small, Minchev et al. (2018) proposed a method to determine the stellar birth radii based on age and metallicity. Briefly, the method assumes that the ISM has a radial metallicity gradient of -0.15 dex kpc^{-1} at the beginning of the disc formation, and monotonically flattens to -0.07 dex kpc^{-1} at present. The ISM metallicity at solar radius is assumed to vary from [Fe/H] ~ -1.0 dex at 13 Gyr ago to 0.1 dex at present. With this prior knowledge, the birth radius of a star can then be derived from its age and [Fe/H].

Furthermore, the effectiveness of this method has been verified by Chen et al. (2019b) by applying it to the LAMOST stars. Similar to Chen et al. (2019b), here we adopt the Minchev et al. (2018) method to estimate the birth radii of our RGB stars. Note that the thick disc stars are widely suggested to exhibit an insignificant radial

metallicity gradient, which is explained as evidence that the disc stars are born from radially well-mixed gas (e.g. Cheng et al. 2012; Boeche et al. 2013; Haywood et al. 2013; Xiang et al. 2015b; Wang et al. 2019a). The birth radii inferred from age and metallicity might be problematic. Therefore, we focus only on the thin disc stars, for which the method applies.

We select the thin disc stars through the [Fe/H]–[α/Fe] plane. The distribution of our RGB stars in the [Fe/H]–[α/Fe] plane is shown in the left-hand panel of Fig. 13. The figure clearly displays two prominent sequences of stars that correspond to the high-α thick disc sequence and low-α thin disc sequence, respectively. We adopt the line shown in the left-hand panel of Fig. 13 as a criterion to distinguish the thin or thick disc stars. The right-hand panel of Fig. 13 suggests that the selected thin disc stars are located in the regions of the age–[Fe/H] plane where the stars have small J_R values, verifying the effectiveness of the selection criteria.

In Fig. 14, we plot the distribution of the difference between the guiding-centre radii and the birth radii $R_g - R_b$ of the thin disc stars in the age–metallicity and R–Z planes. $R_g - R_b$ is a direct measurement of the effection of stellar redistribution due to radial migration. The figure suggests that relatively old stars with super-solar metallicities show positive $R_g - R_b$ values, which means that they are outward migrators from the inner disc. The younger, metal-poor stars show negative $R_g - R_b$ values, indicating that they are inward migrators from the outer disc. At a given age from 4 to 12 Gyr, the maximal difference between R_g and R_b could reach 5 kpc for the most metal-
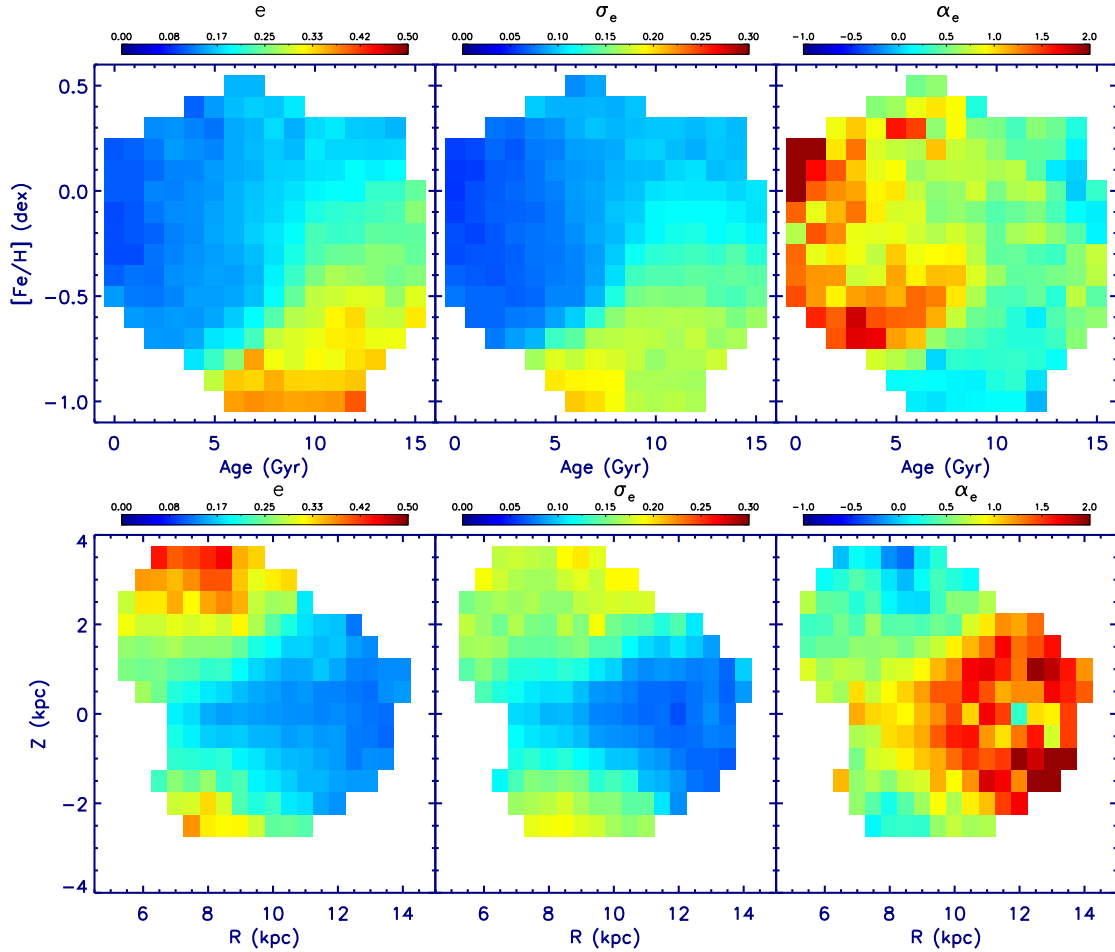
Figure 10. Top panels: colour-coded distributions of median (left), dispersion (middle) and skewness (right) of the eccentricity distribution functions for stars in individual age–[Fe/H] bins of 1 Gyr × 0.1 dex. Bottom panels: colour-coded distributions of median (left), dispersion (middle) and skewness (right) of the eccentricity distribution functions for stars in individual R–Z bins of 0.5 × 0.5 kpc².

rich stars, indicating that these stars may have a minimal average migration speed of about 0.5–1 kpc Gyr^{-1}, if we assume that the stars start to migrate once they are born. This is consistent with Quillen et al. (2018) and Chen et al. (2019b), who suggest that stellar migration due to the excitation of the Galactic bar has a speed of 0.5–1 kpc Gyr^{-1}, depending on the pitch angle of the bar. Interestingly, the data exhibit a lack of stars with [Fe/H] $\gtrsim 0.3$ dex and ages younger than 4 Gyr. For the most metal-poor stars at ages younger than 2 Gyr, the distance of inward migration could reach 4–5 kpc, suggesting a fast migration speed of more than 2 kpc Gyr^{-1}. We do not fully understand such a large migration speed. It is possible that such a fast migration speed might be related to some violent processes, such as perturbations of galaxy mergers. However, it is also possible that the R_b estimates for these outer disc stars suffer large uncertainties.

Fig. 14 further shows the alteration in the median distance due to the radial migration for stars at different positions across the disc R–Z plane. It suggests that, at around the solar radius (7 < R < 9 kpc), the alteration in the median distance is only 0–1 kpc. For stars older than 8 Gyr, the redistribution effect due to radial migration is much stronger, with a median value of 3 kpc. In the outer disc of 9<R <12 kpc, the alteration in the median distance due to the stellar migration for the overall sample stars is small, from −1 to 0 kpc, but the young stars show a larger overall inward migration of −3 kpc.

However, a small alteration in the radial position for the overall stars does not mean a weak migration effect. In fact, Fig. 15 shows that stars with common birth radii show strong migrations. Particularly, for stars born at 12 kpc, very few of them remain at their birth place, but most of them have migrated inward by a large distance (>2 kpc). Such a net inward migration effect might be driven by splashes triggered by merger events of satellite galaxies at the outer disc. Particularly, this figure shows an age stratification for these inward migrators, which is possibly evidence suggesting that the migration in the outer disc was triggered by merger events that have lasted for the past few Gyr. This provides constraints on our understanding of the merger history of our Galaxy (e.g. Minchev, Chiappini & Martig 2016).

The determination of the birth radius depends on assumptions on the time-dependent radial metallicity gradient of the ISM. In order to understand possible uncertainties raised by this assumption, we test different ISM gradients by adopting the mono-age stellar metallicity gradients of Xiang et al. (2015a; see their fig. 15) as an approximation of the ISM gradients. The comparison of the ISM metallicity adopted in this work for the birth radius calculation (i.e. from Minchev et al. 2018) and that of Xiang et al. (2015a) is shown in Fig. 16. The figure also shows the comparison of the birth radius derived from these metallicity gradients, as well as the current position of R_b =
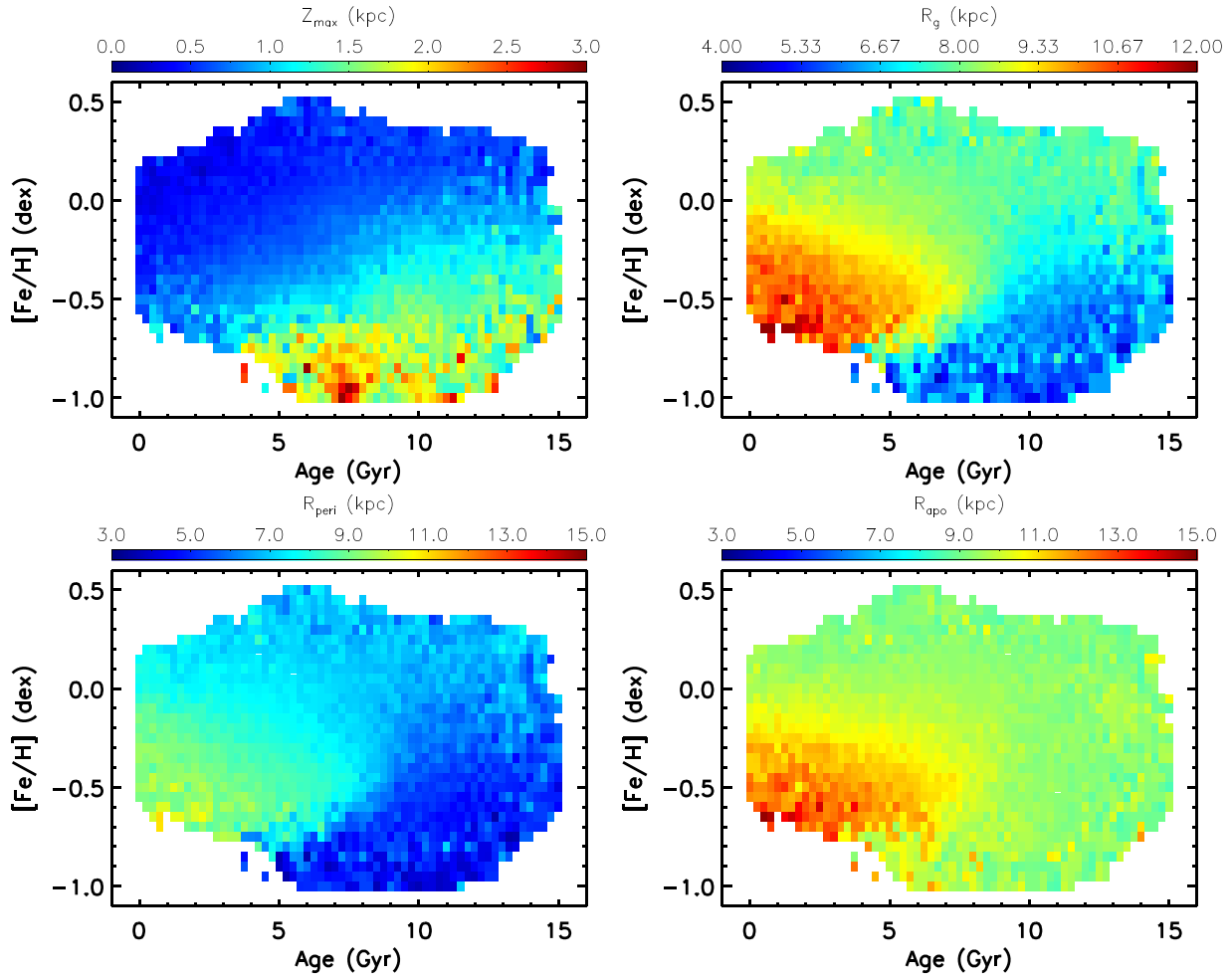
Figure 11. Distributions of the maximal height Z_{max}, guiding-centre radius R_g, pericentre radius R_{peri} and apocentre radius R_{apo} of the stellar orbits across the age–[Fe/H] plane. Colours represent the median values of the orbital parameters for stars in individual age–[Fe/H] bins of $0.25\,\text{Gyr} \times 0.05\,\text{dex}$.
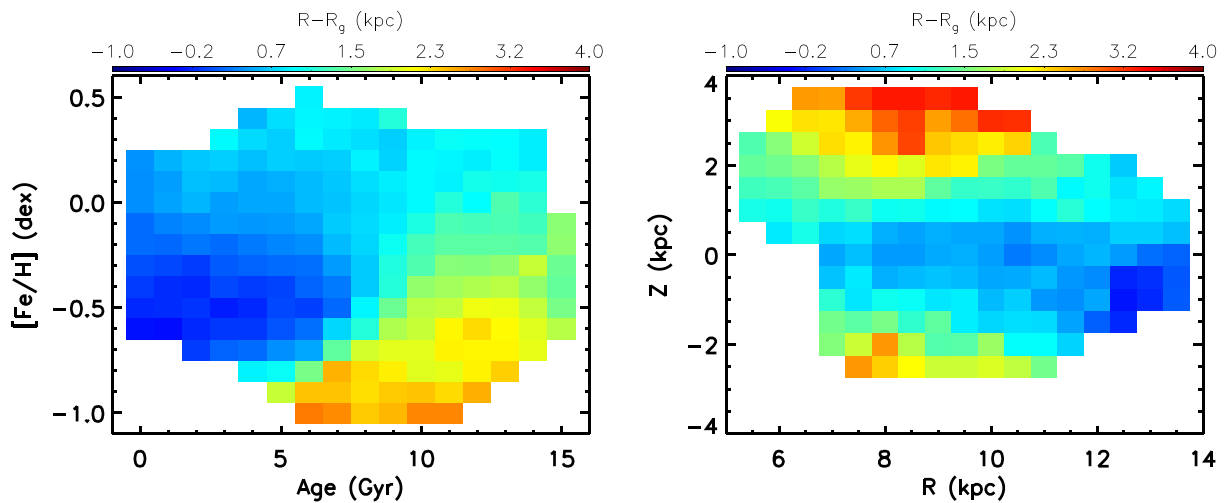

Figure 12. Distributions of $R - R_g$ across the age–[Fe/H] (left-hand panel) and the Galactic R–Z (right-hand panel) planes. Colours represent the median values of $R - R_g$ for stars in individual age–[Fe/H] and R–Z bins.
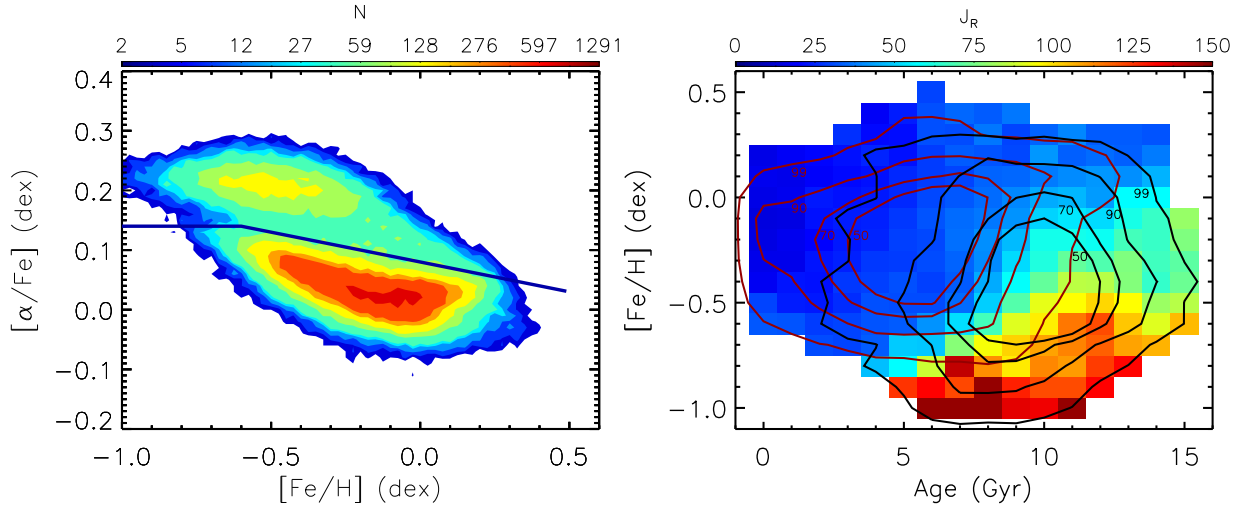
Figure 13. Left-hand panel: [α/Fe] versus [Fe/H] diagram for our RGB sample. The blue solid line delineates the demarcation of the thin and thick disc sequences adopted by this work. Right-hand panel: [Fe/H] versus age diagram for our RGB sample stars, colour-coded by values of J_R. Also shown are the contours indicating 50, 70, 90 and 99 per cent of the selected thin disc (red) and thick disc (black) stars.
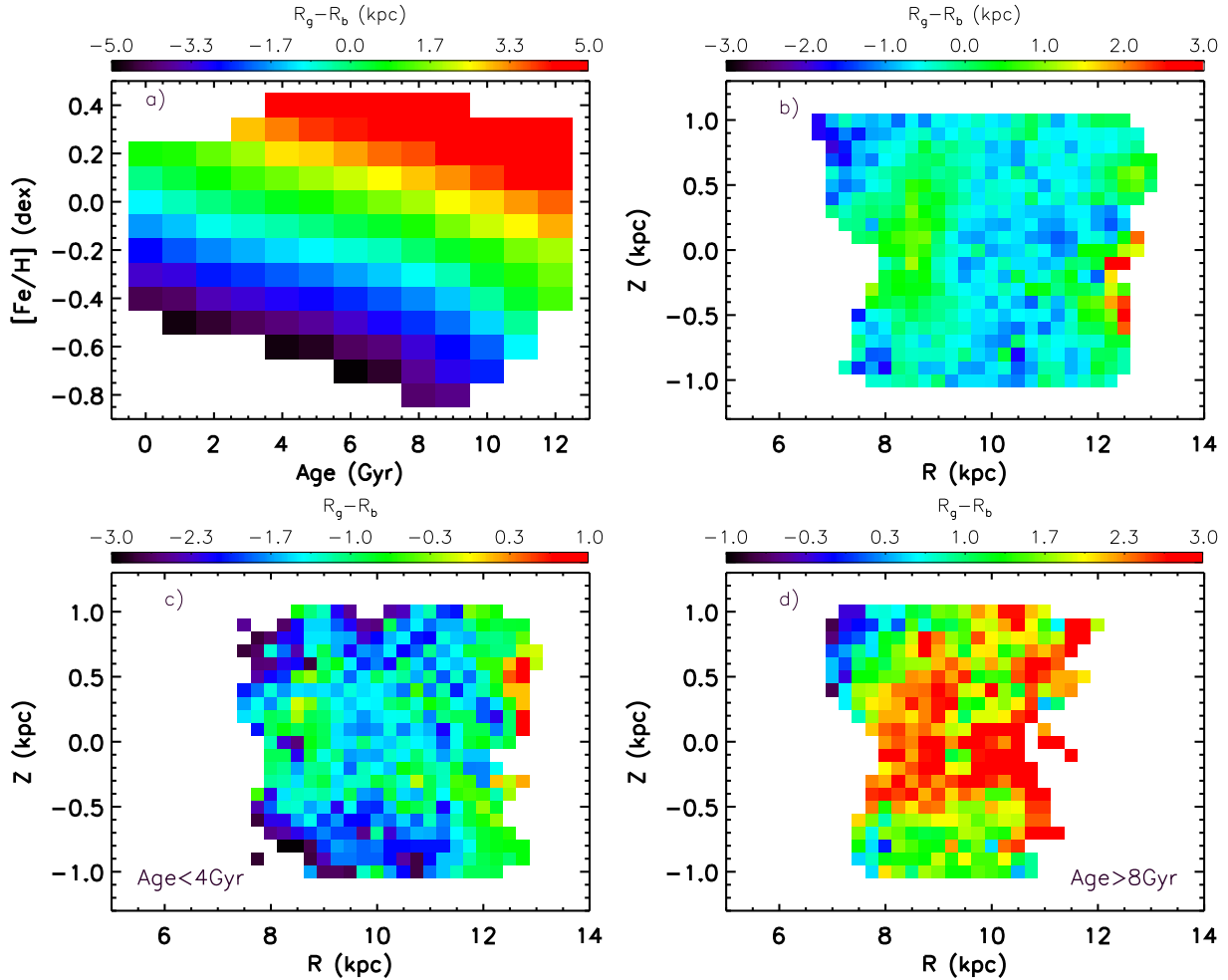
Figure 14. (a) Colour-coded distribution of $R_g - R_b$ for the thin disc stars in the age–[Fe/H] plane. (b) Colour-coded distribution of $R_g - R_b$ for the thin disc stars in the Galactic R–Z plane. (c) Same as (b), but for stars younger than 4 Gyr. (d) Same as (b), but for stars older than 8 Gyr.
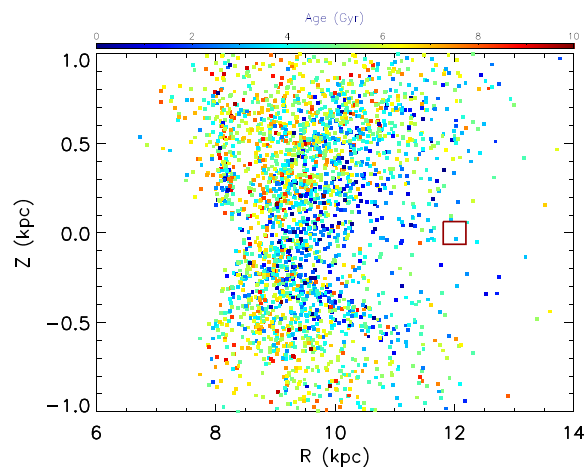
Figure 15. Distributions in the *R–Z* plane for stars born at 12 kpc ($R_b = 12$ kpc), as indicated by the red box. The colour represents stellar age. The stratification effect in stellar age is visible.

12 kpc stars according to the metallicity gradients of Xiang et al. (2015a). The results suggest that our conclusion about the migration is robust (i.e. the results are not significantly affected by the adopted metallicity gradients). This is consistent with the findings of Feltzing, Bowers & Agertz (2020), who have shown that the birth radii of stars with different ages depend only marginally on the adopted ISM metallicity gradients. This confirms the effectiveness of the Minchev et al. (2018) method for estimating stellar birth radii.

5 SUMMARY

We have investigated the stellar kinematics of the Galactic disc in $7 < R < 13$ kpc with a large sample of RGB stars combining LAMOST and *Gaia*. We characterize the median, dispersion and skewness of the distributions of the 3D stellar velocities, actions and orbital parameters across the age–metallicity and the disc *R–Z* planes. We have discussed the impact of stellar migration for thin disc stars by comparing the guiding-centre radii and the birth radii, which

are derived based on age and [Fe/H]. The results reveal abundant kinematic trends and structures. Particularly, we find the following.

(i) The most prominent feature is the clear difference in the velocity and action distributions between the thin and thick disc stars. In the age–[Fe/H] plane, the kinematics exhibit a sharp border between the young, metal-rich thin disc stars and the old, metal-poor thick disc stars. This is particularly clear in the distributions of the actions, and is present in the median, dispersion and skewness for all the 3D actions J_R, J_ϕ and J_Z. The kinematic distinction between the thin and thick disc stars is consistent with the chemical distinction in the [Fe/H]–[α/Fe] plane. These results support the widely accepted suggestion that the Milky Way disc is composed of two major components that are related to different formation and evolution history.

(ii) The velocity distributions reveal several known kinematic substructures in the outer disc. Among them, we confirm the existence of the north–south asymmetries for V_R, which present for stars of all ages and exhibit complicated patterns in the *R–Z* planes. As a part of these complicated patterns, the high-velocity stream at $R \sim 11$ kpc and $Z \sim 0.5$ kpc is also shown in stars of all ages, and is particularly strong for young populations. The data also reveal the north–south asymmetries in V_Z (and V_ϕ) for $R > 10$ kpc, which is the kinematic feature of the disc warp in the outer disc.

(iii) The skewness of the distributions of both V_ϕ and J_ϕ reveals a new substructure at $R \sim 12$ kpc and $Z \sim 0$ kpc, which is related to stars in between the spiral arms (the Perseus arm and the outer arm) in the outer disc. The nature of this substructure deserves to be studied further.

(iv) The thick disc stars have typical guiding-centre radii smaller than 6 kpc, indicating that they are mostly born in the inner disc of $R < 6$ kpc and reach their current positions via highly eccentric orbital motions. The thin disc stars, however, have much smaller eccentricities, which typically lead to only a ∼1 kpc difference between the guiding-centre radii and their current positions. These results are consistent with former works (e.g. Haywood et al. 2013; Kordopatis et al. 2015; Jia et al. 2018).

(v) The old (>4 Gyr), metal-rich stars in our sample exhibit strong outward migration. At a given age, the most metal-rich stars are
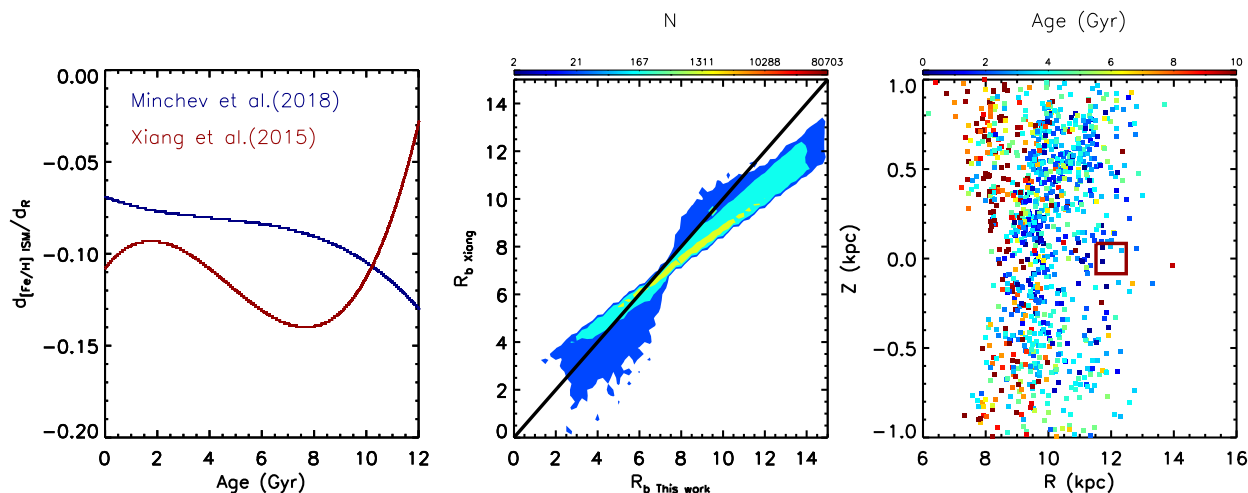
Figure 16. Left-hand panel: comparison of the fits to the evolution functions of the metallicity gradient of Minchev et al. (2018) with Xiang et al. (2015a; see their fig. 15). Middle panel: comparison of birth radius estimates of this work with the metallicity gradient using Xiang et al. (2015a; see their fig. 15). The black solid line represents the 1 : 1 line. The colour bar represent the number of stars. Right-hand panel: distributions in the *R–Z* plane for stars born at 12 kpc (birth radii are calculated with metallicity gradient using of Xiang et al. 2015a), as indicated by the red box. The colour bar presents stellar age.

outward migrators born more in the inner disc at 5 kpc than their current positions, indicating a mean migration speed of about 0.5–1.0 kpc Gyr^{-1}. The metal-poor thin disc stars exhibit strong inward radial migration. At a given age, the most metal-poor stars might have been born at 3–5 kpc further away from their current positions. For young stars, this suggests a fast mean migration speed, probably triggered by merge events.

(vi) All stars born in the outer disc of $R \gtrsim 12$ kpc may have experienced strong inward migration. The spatial distribution in the R–Z plane for the inward migrators born at a given distance (e.g. 12 kpc) shows an age stratification, possibly evidence that these inward migrators are consequences of splashes triggered by merger events of satellite galaxies that have lasted for the past few Gyr.

DATA AVAILABILITY

The data underlying this article will be shared on reasonable request to the corresponding author.

REFERENCES

Adibekyan V. Z. et al., 2013, A&A, 554, A44
Allende Prieto C., Kawata D., Cropper M., 2016, A&A, 596, A98
Anders F., Chiappini C., Santiago B. X., Matijevič G., Queiroz A. B., Steinmetz M., Guiglion G., 2018, A&A, 619, A125
Anders F. et al., 2017, A&A, 600, A70
Antoja T. et al., 2018, Nature, 561, 360
Aumer M., Binney J., 2017, MNRAS, 470, 2113
Aumer M., Binney J., Schönrich R., 2017, MNRAS, 470, 3685
Aumer M., Binney J. J., 2009, MNRAS, 397, 1286
Bailer-Jones C. A. L., Rybizki J., Fouesneau M., Mantelet G., Andrae R., 2018, AJ, 156, 58 (BJ18)
Bensby T., Feltzing S., Lundström I., 2003, A&A, 410, 527

Binney J., Tremaine S., 2008, Galactic Dynamics, 2nd edn. Princeton University Press, Princeton, NJ
Bland-Hawthorn J. et al., 2019, MNRAS, 486, 1167
Boeche C. et al., 2013, A&A, 559, A59
Bovy J., 2015, ApJS, 216, 29
Bovy J., Rix H.-W., Hogg D. W., Beers T. C., Lee Y. S., Zhang L., 2012b, ApJ, 755, 115
Bovy J., Rix H.-W., Liu C., Hogg D. W., Beers T. C., Lee Y. S., 2012a, ApJ, 753, 148
Carlin J. L. et al., 2013, ApJ, 777, L5
Carrillo I. et al., 2018, MNRAS, 475, 2679
Cheng J. Y. et al., 2012, ApJ, 746, 149
Chen X., Wang S., Deng L., de Grijs R., Liu C., Tian H., 2019a, Nature Astron., 3, 320
Chen Y. Q., Zhao G., Zhao J. K., Liang X. L., Wu Y. Q., Jia Y. P., Tian H., Liu J. M., 2019b, AJ, 158, 249
Chequers M. H., Widrow L. M., Darling K., 2018, MNRAS, 480, 4244
Chiba M., Beers T. C., 2000, AJ, 119, 2843
Coronado J., Rix H.-W., Trick W. H., El-Badry K., Rybizki J., Xiang M., 2020, MNRAS, 495, 4098
Curir A., Lattanzi M. G., Spagna A., Matteucci F., Murante G., Re Fiorentin P., Spitoni E., 2012, A&A, 545, A133
Curir A., Mazzei P., Murante G., 2004, in Block D. L.et al. (eds), ASSL Vol. 319, Penetrating Bars through Masks of Cosmic Dust: The Hubble Tuning Fork Strikes a New Note. Kluwer, Dordrecht, p. 335
Deng L-C. et al., 2012, Res. Astron. Astrophys., 12, 735
De Silva G. M. et al., 2015, MNRAS, 449, 2604
Dobbie P. S., Warren S. J., 2020, Open Journal of Astrophysics, 3, 5
Eilers A.-C., Hogg D. W., Rix H.-W., Frankel N., Hunt J. A. S., Fouvry J.-B., Buck T., 2020, ApJ, 900, 186
Feltzing S., Bowers J. B., Agertz O., 2020, MNRAS, 493, 1419
Feuillet D. K., Frankel N., Lind K., Frinchaboy P. M., García-Hernández D. A., Lane R. R., Nitschelm C., Roman-Lopes A. R., 2019, MNRAS, 489, 1742
Frankel N., Rix H.-W., Ting Y-S., Ness M., Hogg D. W., 2018, ApJ, 865, 96
Freeman K., Bland-Hawthorn J., 2002, ARA&A, 40, 487
Gaia Collaboration et al., 2016a, A&A, 595, A1
Gaia Collaboration et al., 2016b, A&A, 595, A2
Gaia Collaboration et al., 2018, A&A, 616, A1
Gilmore G., Reid N., 1983, MNRAS, 202, 1025
Grand R. J. J., Kawata D., 2016, Astron. Nachr., 337, 957
Grieves N. et al., 2018, MNRAS, 481, 3244
Hayden M. R., Recio-Blanco A., de Laverny P., Mikolaitis S., Worley C. C., 2017, A&A, 608, L1
Hayden M. R. et al., 2014, AJ, 147, 116
Hayden M. R. et al., 2020, MNRAS, 493, 2952
Haywood M., Di Matteo P., Lehnert M. D., Katz D., Gómez A., 2013, A&A, 560, A109
Holmberg J., Nordström B., Andersen J., 2009, A&A, 501, 941
Huang Y., Liu X-W., Yuan H-B., Xiang M-S., Chen B-Q., Zhang H-W., 2015, MNRAS, 454, 2863
Huang Y. et al., 2018, ApJ, 864, 129
Jia Y., Chen Y., Zhao G., Xue X., Zhao J., Yang C., Li C., 2018, ApJ, 863, 93
Jing Y. et al., 2016, MNRAS, 463, 3390
Katz D. et al., 2018, A&A, 616, A11
Katz D. et al., 2019, A&A, 622, A205
Kawata D., Baba J., Ciucă I., Cropper M., Grand R. J. J., Hunt J. A. S., Seabroke G., 2018, MNRAS, 479, L108
Kawata D., Grand R. J. J., Gibson B. K., Casagrande L., Hunt J. A. S., Brook C. B., 2017, MNRAS, 464, 702
Kordopatis G. et al., 2013, MNRAS, 436, 3231
Kordopatis G. et al., 2015, MNRAS, 447, 3526
Lee Y. S. et al., 2011, ApJ, 738, 187
Lian J. et al., 2020, MNRAS, 497, 3557
Li C., Zhao G., 2017, ApJ, 850, 25
Lindegren L. et al., 2018, A&A, 616, A2
Liu C., Xue X., Fang M., van de Ven G., Wu Y., Smith M. C., Carrell K., 2012, ApJ, 753, L24

[5]https://www.cosmos.esa.int/gaia
[6]https://www.cosmos.esa.int/web/gaia/dpac/consortium

Liu X. W. et al., 2014, in Feltzing S., Zhao G., Walton N. A., Whitelock P., eds, Proc. IAU Symp. Vol. 298, Setting the Scene for Gaia and LAMOST. Kluwer, Dordrecht, p. 310

Li Z-Y., Shen J., 2020, ApJ, 890, 85

Loebman S. R., Roškar R., Debattista V. P., Ivezić Ž., Quinn T. R., Wadsley J., 2011, ApJ, 737, 8

Mackereth J. T. et al., 2017, MNRAS, 471, 3057

Majewski S. R. et al., 2017, AJ, 154, 94

Minchev I., Chiappini C., Martig M., 2013, A&A, 558, A9

Minchev I., Chiappini C., Martig M., 2016, Astron. Nachr., 337, 944

Minchev I., Martig M., Streich D., Scannapieco C., de Jong R. S., Steinmetz M., 2015, ApJ, 804, L9

Minchev I. et al., 2018, MNRAS, 481, 1645

Ness M. et al., 2018, ApJ, 853, 198

Ness M. K., Johnston K. V., Blancato K., Rix H.-W., Beane A., Bird J. C., Hawkins K., 2019, ApJ, 883, 177

Nordström B. et al., 2004, A&A, 418, 989

Peng X., Wu Z., Qi Z., Du C., Ma J., Zhou X., Jia Y., Wang S., 2018, PASP, 130, 074102

Poggio E. et al., 2018, MNRAS, 481, L21

Quillen A. C., Nolting E., Minchev I., De Silva G., Chiappini C., 2018, MNRAS, 475, 4450

Recio-Blanco A. et al., 2014, A&A, 567, A5

Romero-Gómez M., Mateu C., Aguilar L., Figueras F., Castro-Ginard A., 2019, A&A, 627, A150

Roškar R., Debattista V. P., Quinn T. R., Stinson G. S., Wadsley J., 2008, ApJ, 684, L79

Schönrich R., Binney J., 2009, MNRAS, 396, 203

Sellwood J. A., Binney J. J., 2002, MNRAS, 336, 785

Siebert A. et al., 2011, MNRAS, 412, 2026

Skowron D. M. et al., 2019, AcA, 69, 305

Spagna A., Lattanzi M. G., Re Fiorentin P., Smart R. L., 2010, A&A, 510, L4

Spitoni E., Silva Aguirre V., Matteucci F., Calura F., Grisoni V., 2019, A&A, 623, A60

Steinmetz M. et al., 2006, AJ, 132, 1645

Sun N-C. et al., 2015, Res. Astron. Astrophys., 15, 1342

Tian H-J., Liu C., Wu Y., Xiang M-S., Zhang Y., 2018, ApJ, 865, L19

Tian H-J. et al., 2015, ApJ, 809, 145

Tian H-J. et al., 2017, Res. Astron. Astrophys., 17, 114

Ting Y-S., Rix H.-W., 2019, ApJ, 878, 21

Vrard M., Mosser B., Samadi R., 2016, A&A, 588, A87

Wang C. et al., 2019a, ApJ, 877, L7

Wang H-F., Liu C., Xu Y., Wan J-C., Deng L., 2018b, MNRAS, 478, 3367

Wang H-F., López-Corredoira M., Carlin J. L., Deng L., 2018a, MNRAS, 477, 2858

Wang H-F. et al., 2019b, ApJ, 884, 135

Wang H-F. et al., 2020, ApJ, 897, 119

Widrow L. M., Barber J., Chequers M. H., Cheng E., 2014, MNRAS, 440, 1971

Widrow L. M., Gardner S., Yanny B., Dodelson S., Chen H-Y., 2012, ApJ, 750, L41

Williams M. E. K. et al., 2013, MNRAS, 436, 101

Wojno J. et al., 2018, MNRAS, 477, 5612

Wu Y. et al., 2018, MNRAS, 475, 3633

Wu Y. et al., 2019, MNRAS, 484, 5315

Xiang M-S. et al., 2015a, Res. Astron. Astrophys., 15, 1209

Xiang M-S. et al., 2015b, MNRAS, 448, 822

Xiang M-S. et al., 2017a, ApJS, 232, 2

Xiang M-S. et al., 2017b, MNRAS, 467, 1890

Xiang M-S. et al., 2018, ApJS, 237, 33

Xu Y., Newberg H. J., Carlin J. L., Liu C., Deng L., Li J., Schönrich R., Yanny B., 2015, ApJ, 801, 105

Yanny B. et al., 2009, ApJ, 700, 1282

Yan Y., Du C., Liu S., Li H., Shi J., Chen Y., Ma J., Wu Z., 2019, ApJ, 880, 36

Yuan H. B. et al., 2015, MNRAS, 448, 855

Zhao G., Chen Y-Q., Shi J-R., Liang Y-C., Hou J-L., Chen L., Zhang H-W., Li A-G., 2006, Chin. J. Astron. Astrophys., 6, 265

Zhao G., Chen Y., 2020, preprint (arXiv:2012.01282)

Zhao G., Zhao Y-H., Chu Y-Q., Jing Y-P., Deng L-C., 2012, Res. Astron. Astrophys., 12, 723

APPENDIX

Fig. A1 shows an example of the one-dimensional distribution of V_R, J_R, V_ϕ, J_ϕ, V_Z and J_Z for different age and metallicity bins. In particular, we select two age and metallicity bins, and we mark the value of skewness of these distributions in the figure.

Fig. A2 shows the distributions at different birth radii in the R–Z plane. We select three regions of birth radii to validate the alteration in the median distance due to the radial migration shown in Fig. 15. From Fig. A2, we can see that for stars born beyond 10 kpc, the results are consistent with Fig. 15, whereas stars in the outer disc show a much stronger inward migration effect. This might be caused by the stronger interactions with satellite galaxies at the outer disc.
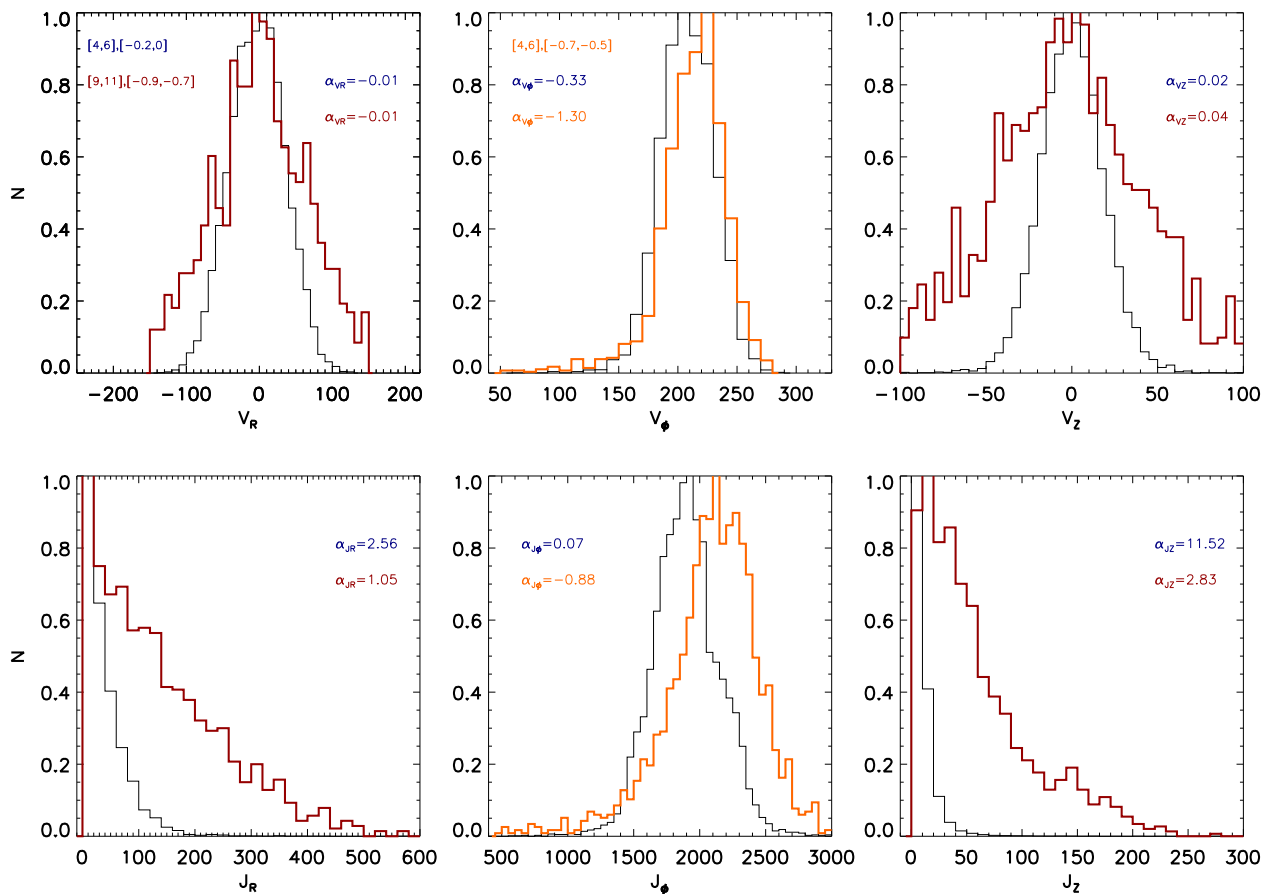
Figure A1. One-dimensional distribution of V_R, J_R, V_ϕ, J_ϕ, V_Z and J_Z for different age bins and metallicity bins. The black line represents $4 < \tau < 6$ Gyr, $-0.2 < $ [Fe/H] $ < 0$, and the red line represents $9 < \tau < 11$ Gyr, $-0.9 < $ [Fe/H] $ < -0.7$ dex. Distributions with positive tails exhibit positive values of skewness, while distributions with negative tails exhibit negative values of skewness.
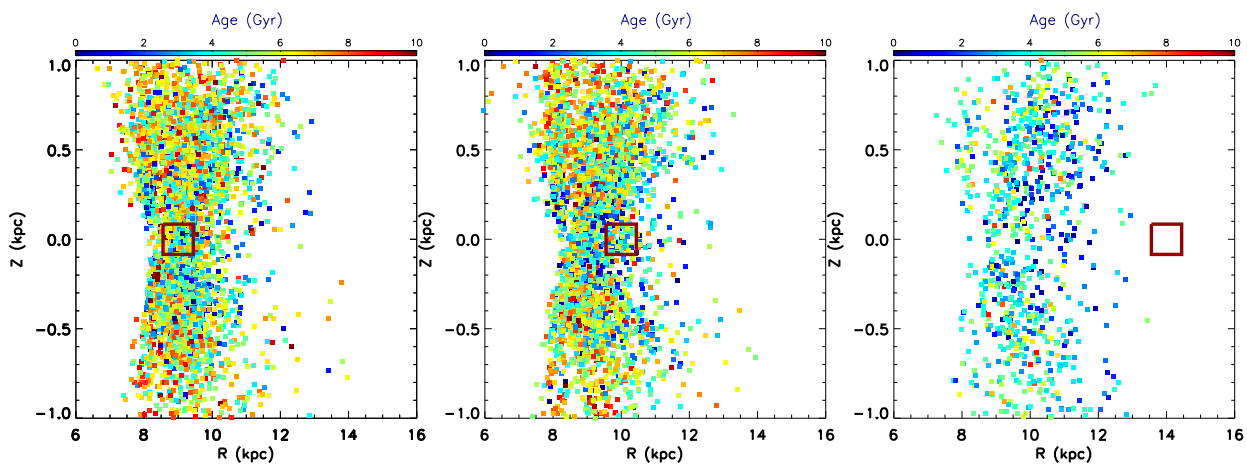
Figure A2. Distributions in the R–Z plane for stars born at 9, 10 and 14 kpc (from left to right), as indicated by the red box. The colour represents stellar age.

This paper has been typeset from a TEX/LATEX file prepared by the author.